CARRIER PHASE MULTIPATH CHARACTERIZATION AND FREQUENCY-DOMAIN BOUNDING

BY

CHLOÉ BENZ

Submitted in partial fulfillment of the
requirements for the degree of
Master of Science in Autonomous Systems and Robotics
in the Graduate College of the
Illinois Institute of Technology

Approved _____
Adviser

Chicago, Illinois
May 2022

ACKNOWLEDGEMENT

First and foremost, I would like to express my heartfelt gratitude to my advisor and thesis defense committee member Pr. Boris Pervan for welcoming me in the Navigation Laboratory at Illinois Institute of Technology and providing thorough explanations and insightful comments throughout my time spent working there. The knowledge I built from this experience I am sure will stick with me through my career.

I am also grateful for Elisa Gallon's help during the time I spent working on my Master's thesis, and for the work she put in to get me onboard, to support me along the way, and to suggest corrections to improve my writing.

I wish to also thank the rest of my thesis defense committee Pr. Seebany Datta-Barua and Pr. Carrie Hall, for their time and thoughtful comments.

Finally, I would like to thank my best friends Arthur Findelair, Marie Keime and Tom Bachard, who took some time in their schedule to proof-read my work (and learn new things in the process).

AUTHORSHIP STATEMENT

I, Chloé Benz, attest that the work presented in this thesis is substantially my own.

In accordance with the disciplinary norm of Mechanical, Materials and Aerospace Engineering (see IIT Faculty Handbook, Appendix S), the following collaborations occurred in the thesis:

Pr. Boris Pervan of Illinois Institute of Technology contributed to the design of all experiments and assisted and guided in the interpretation of all data and derivations as is the norm for a Master's thesis supervisor. He also provided ground work, cited where relevant in this thesis.

Elisa Gallon, Ph.D. candidate at Illinois Institute of Technology, collaborated on the writing of the MATLAB codes developed and forked in this work for ionospheric delay estimation. She provided ground work, cited where relevant in this thesis. She also made available to me the GPS carrier phase data used in Chapter 4, that she collected during the year 2020.

Dr. Stefan Stevanovic, formerly of Illinois Institute of Technology, Chicago, IL, provided the base Fortran and MATLAB codes from one of his previously published work, which were modified and built upon for this work for ionospheric delay estimation. Said previous work is cited where relevant in this thesis.

TABLE OF CONTENTS

LIST OF TABLES

LIST OF FIGURES

LIST OF SYMBOLS

Symbol	Definition
c	Speed of light in vacuum
ϕ	Carrier phase
r	Range
b	Clock bias
T	Tropospheric delay
I	Ionospheric delay
λ	Wavelength
ν	Multipath
σ^2	Variance
$q^{t(f)}_{a(s)}$	Physical quantity q at time t, measured at antenna a and sent by satellite s on frequency f
$q^{t(f)}_{a_1-a_2(s)}$	$q^{t(f)}_{a_1(s)}$ - $q^{t(f)}_{a_2(s)}$
$q^{t(f)}_{a(s_1-s_2)}$	$q^{t(f)}_{a(s_1)}$ - $q^{t(f)}_{a(s_2)}$
$q^{t(f_1-f_2)}_{a(s)}$	$q^{t(f_1)}_{a(s)}$ - $q^{t(f_2)}_{a(s)}$
$\overline{q}$	Constant physical quantity q

LIST OF ABBREVIATIONS

Abbreviation	Term
ABAS	Aircraft-Based Augmentation System
ACF	Autocorrelation Function
ARAIM	Advanced Receiver Autonomous Integrity Monitoring
C/A	Coarse acquisition (code)
DA	Dual Antenna
DF	Dual Frequency
GBAS	Ground-Based Augmentation System
GMRP	Gauss-Markov Random Process
GNSS	Global Navigation Satellite System
GPS	Global Positioning System
INS	Inertial Navigation System
IMU	Inertial Measurement Unit
KF	Kalman Filter, Kalman Filtering
K-S	Kolmogorov-Smirnov (2 samples stationarity test)
LS	Lomb-Scargle (periodogram)
LoS	Line of Sight
NLoS	Non Line of Sight
NSS	Navigation Satellite System
P	Precision (code)
PNT	Positioning, Navigation and Timing
PRN	Pseudo-Random Noise (code)

PSD	Power Spectral Density
RAIM	Receiver Autonomous Integrity Monitoring
RegNSS	Regional Navigation Satellite System
SBAS	Satellite-Based Augmentation System
TEC	Total Electron Content

ABSTRACT

Safely relying on Global Navigation Satellite Systems (GNSS) measurements for position estimation using multi-sensor navigation algorithms, especially in critical phases of flight – such as takeoff or landing – requires precise knowledge of the errors affecting position estimates and their extrema values at any time. This work investigates a method for characterization and power-spectral density (PSD) bounding of GNSS carrier phase multipath error intended for use in sensor fusion for aircraft navigation. In this dissertation, two methods of GNSS carrier phase multipath characterization are explored: single frequency dual antenna (DA) and single antenna dual frequency (DF). However, since not all aircraft are equipped with multiple GNSS antennas, because the DA method entails a meticulous tracking of the lever arm between the two antennas, and as multipath seen by two antennas in a short baseline configuration may cancel out, the DF method is preferred and is the main emphasis of this work. By subtracting carrier phase measurements collected by a receiver over two distinct frequencies, a composite measurement containing ionospheric delay and carrier phase multipath is obtained. The ionospheric delay has slower dynamics than multipath, so it is removed using a high pass filter. The filter cutoff frequency is carefully picked based on a study of ionospheric delay dynamics. The DF method is validated on a rooftop GPS carrier phase dataset, and finally, directions and considerations for its ultimate intended use on airborne collected GNSS carrier phase data are provided.

CHAPTER 1

INTRODUCTION

1.1 Navigation Satellite Systems

With mankind's growing ability to explore the world – and now the universe – with different means, arose the need for positioning and navigation capabilities. However, those needs evolved considerably from the time they were expressed. If a mere map, mechanical watch and compass were sufficient to first navigate the continents, seas and oceans, today's applications – especially with the rise of autonomous vehicles – require high precision and accuracy that cannot be achieved with these simple tools. Luckily, this past century has witnessed many scientific breakthroughs, that led to significant improvements in the navigation community – such as the development of Navigation Satellite Systems (NSS), and especially Global Navigation Satellite Systems (GNSS). A GNSS is defined as a satellite constellation that has its own independent Positioning, Navigation and Timing (PNT) capabilities and provides global coverage. Through the broadcast of a navigation message, GNSS provide all the necessary information for GNSS-able receivers to estimate their three dimensional position on Earth.

The main four GNSS, all operational at the time of the writing of this thesis, are summed up in the first section of Table 1.1. In the second section, non-global NSS are mentioned, under the name Regional NSS (RegNSS). Those systems provide local PNT capabilities to their countries of origin, who sometimes lack decent GNSS coverage. Note that QZSS referenced in Table 1.1 is currently considered as a Satellite-Based Augmentation System (SBAS), with plans to make it an independent RegNSS for the future. To put it simply, SBAS work by receiving and re-broadcasting GNSS correction messages from ground stations. SBAS cannot provide positioning services on their own – they only help improving accuracy and integrity of GNSS.

Table 1.1. Operational NSS overview

	Full designation	Abbr.	Origin
GNSS	Global Positioning System	GPS	U.S.A.
	Globalnaya Navigazionnaya Sputnikovaya Sistema	GLONASS	Russia
	BeiDou Navigation Satellite System	BDS	China
	Galileo	N/A	E.U.
RegNSS	Quasi-Zenith Satellite System	QZSS	Japan
	Navigation with Indian Constellation	NavIC	India

Only GPS data is used in this work (see Chapter 4), but carrier phase multipath affects all constellations similarly, so the methodology described in this report is applicable to other GNSS constellations as well. The principle of GPS receivers is to estimate position information using pseudorange multilateration. A visual is provided on Figure 1.1 for two dimensional multilateration. The idea is that a user can compute its range with regard to each satellite from the GNSS signals it receives. The range is computed from the measured time of arrival of the GNSS signal at the receiver, and the time of departure of said GNSS signal contained in the navigation message modulated onto the signal. In theory, for a user to compute its position by multilateration, at least two line of sight (LoS) satellites are necessary in two dimensions, and three in three dimensions [1]. An additional satellite is required to account for the fact that all clocks involved to determine time of departure and time of arrival of signals are not perfectly synchronized – adding an incertitude on the travel time, and therefore on the range estimation (symbolized by the dashed lines on Figure 1.1). Range information in three dimensions defines a sphere on which the user could be – whereas it only defines a circle of possible positions in two dimensions. Accounting

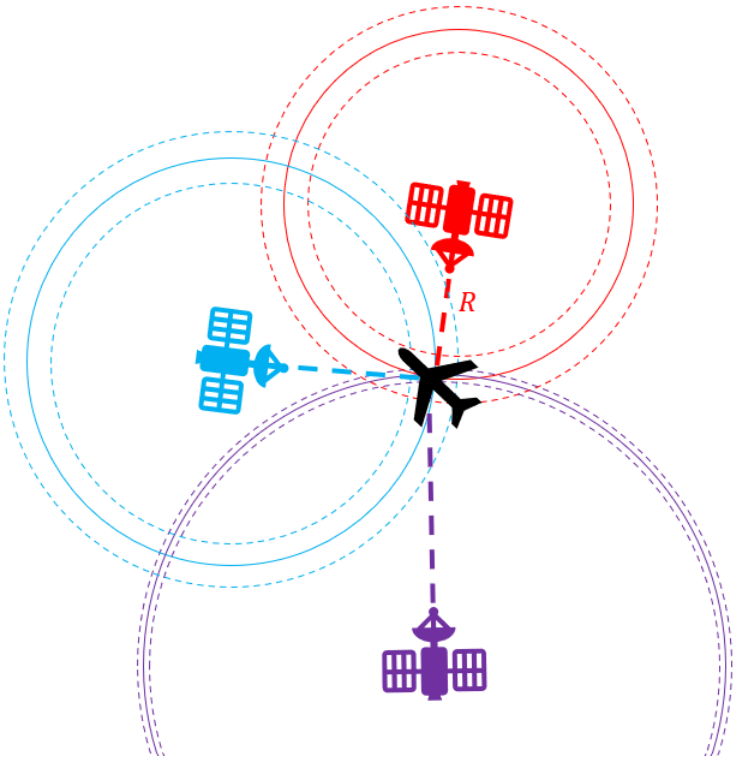

Figure 1.1. 2D multilateration example

for the time incertitude, in three dimensions, the position could be anywhere in a spherical shell. In practice, there are often more than four LoS satellites, and therefore, redundant measurements, which is great for error minimization. Non line of sight satellites (NLoS) are the satellites not directly in view of the receiver and thus, should not be used for multilateration.

1.2 Integrity and improving performances

In safety critical applications, like aircraft navigation where many lives are at stake, it is essential to ensure the integrity of the information used to estimate position. Integrity can be defined as a measure of the trust that can be put in the correctness of the navigation information supplied by a third party – in this case, GNSS. Integrity has a definition close to that of accuracy, but is more stringent. In addition, integrity encompasses the ability to issue warnings in a timely manner

when measurements are compromised. The three main structures that can provide GNSS integrity [2] are: SBAS (previously mentioned), as well as Ground-Based Augmentations Systems (GBAS) and Aircraft-Based Augmentation Systems (ABAS). Receiver Autonomous Integrity Monitoring (RAIM), and more recently, Advanced Receiver Autonomous Integrity Monitoring (ARAIM), are ABAS mostly meant for aircraft navigation. The advantage is that RAIM/ARAIM are performed onboard an aircraft, and can therefore can provide self-integrity for a plane using GNSS-aided navigation, even outside SBAS/GBAS coverage areas. Historically, the RAIM technology only uses GPS L1 signals, and was meant for horizontal navigation in non critical phases of flight. ARAIM, an improvement of the RAIM technology, is currently being designed for GNSS inter-operability, for both horizontal and vertical navigation, including during critical phases of flight, such as takeoff and landing of the aircraft. These technologies are robust against drifting and allow for improved accuracy on position estimates compared to GNSS alone. However, when used with GNSS only, they are sensitive to radio frequency interferences (jamming, spoofing) – a drawback that can be alleviated using sensor fusion algorithms.

1.3 Sensor fusion

For further improved precision and accuracy in position estimation, as well as protection against radio frequency interference, GNSS measurements are often used in combination with measurements from other sensors in what is called sensor fusion algorithms in the literature. In air navigation, for instance, GNSS receivers are often used along with Inertial Navigation Systems (INS) such as Inertial Measurement Units (IMU), radars and radio-based ranging systems. In safety critical applications, measurements are generally combined using Kalman Filters (KF) – since those account for noise and errors and can be used dynamically and in real-time. Another huge advantage from the use of a KF is that it combines measurements from multiple sensors to estimate a state and its covariance. These measurements can include errors

(noise), which is always the case in practice. KF algorithms are based on weighting the measurements they get as input based on a predefined knowledge of the measurement error characteristics. Hence, to safely use KF fed with GNSS measurements in air navigation, accurate error models are needed for all errors impacting GNSS measurements. Further, stochastic error models that account for error dynamics are needed for ARAIM.

1.3.1 Main sources of errors. In GNSS measurements, there are four main sources of error:

- **Orbit** – the orbit of the satellite is only known to certain degrees of precision and confidence, which reflects on the estimation of the satellite-user range
- **Clock** – the satellite clocks are not perfectly synchronized and are prone to drifting, which can cause significant errors
- **Atmoshperic** – the refraction of the signals by the tropospheric and ionospheric layers of the atmosphere cause the signal propagation delays
- **Multipath** – satellite signals reflections cause extended signal travel time

This thesis provides background to characterize multipath, a common error source in GNSS. In the process of developing a single user carrier phase multipath characterization method, ionospheric delay is also investigated.

1.3.2 Multipath. Multipath is a radio frequency wave propagation phenomenon that results in an antenna receiving a signal from one single source via multiple distinct paths. Figure 1.2 provides a visual explanation of this phenomenon for a GNSS antenna embedded in a car in an urban environment. Note that GNSS signals are usually transmitted in the form of a main beam pointing towards the center of the Earth [3]. With a focused and perfectly collimated beam, only either a direct

or a reflected signal from a specific satellite would be received by an antenna. But in the real case, with a large, conic broadcast beam (in green on Figure 1.2), one single LoS satellite can generate both direct and reflected radio waves received by the same antenna. This means that a single antenna can receive both direct and reflected signals from the same satellite. In addition, the reflections can occur on multiple objects of the environment.

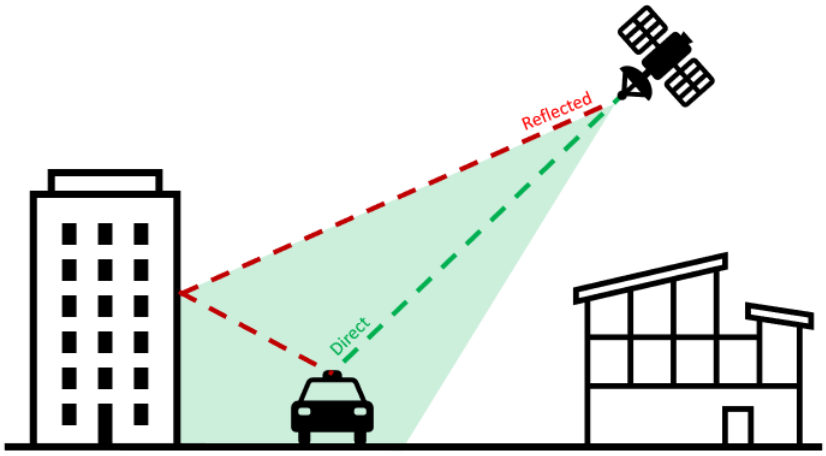

Figure 1.2. Ground multipath example

As mentioned in the previous section, multipath is due signal reflections on the environment, causing extended signal travel time. As a result, the time of arrival of the signal, used for the computation of the satellite-antenna range, is longer than what it should be in the no reflection case – which leads to an incorrect estimation of the range. Multipath error depends on the direct environment the GNSS signals travel in. A receiver embedded in a ground vehicle travelling in an urban area would for instance measure multipath from reflections of the GNSS signals on the surrounding buildings and infrastructures, as pictured on Figure 1.2. A receiver embedded in an aircraft would however measure multipath error from reflections of the GNSS signals on the wings and fuselage when airborne – superposed to reflections on the runways and airport infrastructures when taking off or landing. The expectations and details

for aircraft multipath will be discussed in Chapter 5. To be able to use GNSS aided navigation in all phases of flight, a precise characterization and upper-bounding of multipath error dynamics is necessary.

1.4 Motivation and contributions

This dissertation focuses on the development of a carrier phase multipath model that accounts for multipath dynamics over time. Specifically, the focal point of this work is the design of a dual frequency (DF) carrier phase multipath error characterization method, to evaluate carrier phase multipath for any single antenna application. A separate dual antenna (DA) method is also considered. Since the DA approach is currently widely accepted for evaluating carrier phase multipath, it is used in this work to serve as a reference for what can be expected of the DF method.

The DF method for carrier phase multipath characterization entails a study of the ionospheric delay dynamics, currently based on simulated ionospheric delay computed using a well known model – the International Reference Ionosphere (IRI) [4]. The DF method and ionospheric delay dynamics study designed in this work are tested on GPS carrier phase measurements, but are ultimately meant for use with other GNSS constellations. This works comes to complement the dynamics models already developed for orbit [5] and tropospheric [6] errors for an ultimate intended use in a KF-based algorithm for a multi constellation ARAIM.

CHAPTER 2

CARRIER PHASE MULTIPATH CHARACTERIZATION

This Chapter introduces GPS signals, and how carrier phase measurements are affected by multipath, since in this work, only GPS carrier phase measurements are used. However, as mentioned earlier, carrier phase multipath is not constellation dependant – it therefore impacts other GNSS carrier phase measurements the same. Also, GNSS adopted signal structures similar to that of GPS. Hence, the methods described in this Chapter also apply to other GNSS, with only small conceptual differences. This Chapter provides the theory behind the methods for the carrier phase multipath characterization methods investigated in this Master's thesis.

2.1 Global Positioning System (GPS) signals

GPS signals are the signals broadcast by the satellites in the GPS constellation to enable GPS receivers to determine their position in the three dimensional space. Not all GPS signals are intended for civilian use, but military signals are not covered in this work (although the concepts presented would be applicable to them as well). The different GPS signals are broadcast using three distinct carrier frequencies [7]. Table 2.1 provides an overview of civilian available GPS signals. They all contain the navigation message, which has information on the current GPS week and time, as well as the satellite's status and orbit, which are essential for position estimation.

Table 2.1. GPS civilian signals overview

	Frequency (MHz)	**Bandwidth (MHz)**	**Civilian available signals**
$L1$	1,575.42	30.69	$L1$ C/A, $L1$C, $L1$P(Y)
$L2$	1,227.60	30.69	$L2$C, $L2$P(Y)
$L5$	1,176.45	24.00	$L5$

Each satellite broadcasts signals that are composed of the navigation data, modulated using a binary modulation technique onto a unique code that can be linked to a specific satellite. Each navigation + code composite signal is then modulated onto a carrier using phase modulation and broadcast towards the Earth. The unique code upon which navigation data is modulated can either be coarse acquisition (C/A) or precise (P) code, for civilian GPS. The C/A code is a Pseudo-Random Noise (PRN) code, which has very low correlation with other PRN codes from the same set, and only strongly autocorrelates when aligned to itself. Since each GPS satellite has its own unique PRN code, from here on, a satellite will be designated using its PRN code number. The GPS PRN code numbers range from 1 to 32, though there are usually less than 32 operational satellites in the GPS constellation at any given time. On another hand, the P code is not unique to a satellite. In fact, each satellite uses a unique portion of the same P code. While the P code is public, what is broadcast is an encrypted version of it, called P(Y), and is meant for military use. Methods exist for civilian tracking of the P(Y) code without knowledge the encryption code. From Table 2.1: $L1$ C/A, $L1$C, $L2$C and $L5$ are PRN code based, while $L1$P(Y) and $L2$P(Y) are P code based signals. Only the most recent recent satellites in the GPS constellation are designed to be able to broadcast all of these signals [8]. However, all operational satellites can broadcast as much of these signals as is allowed by their hardware. This means each satellite has a unique PRN code, and a unique P code section associated to it (as well as unique military codes, not discussed here). The next sections focus on PRN code measurements only, as well as carrier phase measurements from all three GPS carrier frequencies.

2.2 Code and carrier phase measurements

There are two ways to estimate the range between a satellite and a receiver: using code measurements, or using carrier phase measurements. Reference [9] gives a clear and simple explanation of both methods of range estimation. A code estimated

range can be regarded as a distance measured with a labeled ruler of coarse precision – yielding a not so precise but accurate estimation. A carrier phase estimated range, in contrast, can be seen as measured using a very high resolution but unlabeled measurement tape – leading to a very precise but not accurate estimation. Accuracy refers to how close a measurement is to its ground truth value, and precision is a measure of how close the measurements are to each other. Figure 2.1 provides a visual explanation of range estimation using code and carrier phase measurements. Note that this Figure is not to scale ($\lambda^{(L1)} \approx 19$ cm while 1 chip ≈ 293 m).

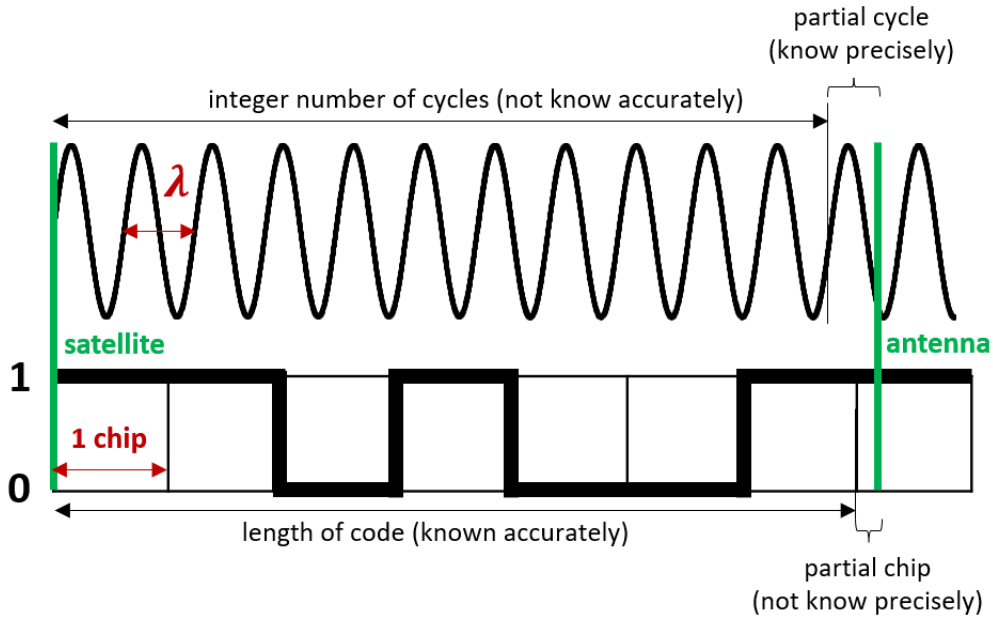

Figure 2.1. Code vs. carrier based range estimation

In more details, for range estimation through code measurements, the receiver compares the PRN received from a satellite to the one it generates locally. The PRN code generated by the receiver is shifted in time until it correlates with the PRN code it received – since PRN codes only strongly autocorrelate when perfectly aligned with themselves. The amount of time by which the code was shifted is the signal pseudo travel time, which is used to compute an estimation of the range. This

way of estimating the range is accurate and unambiguous, but as stated earlier, not very precise, with PRN codes being 1,023 chips long, or about 300 km. The errors for code measurements are contained within one chip of accuracy, or about 293 m. A chip is comparable to the wavelength λ for a carrier wave – except typically, a chip is a rectangular pulse of 0 or 1 of amplitude [10] and does not repeat periodically like a carrier cycle. Figure 2.1 provides a visual representation of what a chip is.

To compute the range with carrier phase measurements, the receiver measures the difference in phase between the received carrier signal and the locally replicated carrier. It is essentially the same principle as with code phase measurements except that with carrier phase, the range is known more precisely, since the error on range estimation is contained within one wavelength λ of accuracy (about 19 cm for $L1$) as opposed to the one chip accuracy (about 293 m) with code. However, the carrier range measurement is less accurate – an ambiguity exists since the number n of whole carrier cycles λ separating the satellite from the antenna is not known with certainty. In essence, the receiver *sees* a certain number of whole cycles, and one partial cycle. It does not know exactly how many whole cycles it has seen, but can measure the partial cycle with precision by measuring the phase. In this work, precision is essential, hence the choice of using carrier phase measurements, though range estimation using code measurements is easier. Another phenomenon that pushes the use of carrier phase measurements instead of code is antenna group delay, that strongly affects code measurements (but not carrier). Also, carrier phase measurements are already widely used in air navigation.

2.3 Carrier phase measurement model

The carrier phase measurement model used throughout this work [9], expressed in units of meters, is the following:

$$\phi_{a(s)}^{k(f)} = r_{a(s)}^{k(s)} + b_{a(s)}^{k(f)} + T_{a(s)}^{k(f)} - I_{a(s)}^{k(f)} + \lambda^{(f)} n_{a(s)}^{k(f)} + \nu_{a(s)}^{k(f)} \tag{2.1}$$

Some sub- and superscripts can be dropped when a quantity is not either time, frequency, antenna or satellite dependent. Table 2.2 references all the contributions to the carrier phase measurement model. These contributions are explained with more details in the next few paragraphs.

Table 2.2. Contributions to the carrier phase measurement model

Notation	**Extended expression**	**Contribution**
$r^k_{a(s)}$		Range
$b^{k(f)}_{a(s)}$	$\frac{c}{\lambda^{(f)}}(\delta t^k_a - \delta t^k_{(s)})$	Clock bias
$T^k_{a(s)}$		Tropospheric delay
$I^{k(f)}_{a(s)}$		Ionospheric delay
$n^{k(f)}_{a(s)}$		Integer cycle ambiguity
$\nu^{k(f)}_{a(s)}$		Multipath and receiver noise

The range designates the distance between the broadcasting satellite s and the receiving antenna a.

The clock bias encompasses the difference between the receiver local time and the satellite time, and is receiver and satellite dependent.

The tropospheric delay is the delay due to the refraction of the signals in the troposphere, a layer of the atmosphere, shelling the Earth. The GNSS signals refract on the dry gases present in the troposphere, but also on the water vapor. While dry gas content dynamics are quite precisely predictable, vapor content depends on the local meteorological conditions, which require extensive modeling. Fortunately, the tropospheric delay is mainly due to the hydrostatic component (refraction on dry gases) [11]. Tropospheric delay is not dependent on carrier frequency, and a

tropospheric delay dynamics model has already been established in reference [6].

The ionospheric delay is the delay due to the refraction of the GNSS signals in the ionosphere, a layer of the atmosphere located above the troposphere, where radiations from solar activity ionize the gaseous content. Present gases ionize into positively charged ions, freeing electrons in the process. The more intense the solar activity, the greater the ionization and the greater the electron content. This nonzero electron content, coupled to the Earth's magnetic field is what makes the ionosphere a dispersive medium – meaning it refracts electromagnetic signals differently depending on their frequency [12]. As a result, the ionospheric delay on GNSS signals is carrier wave frequency dependent, and can reach a few meters in magnitude depending on the latitude and longitude of the receiving antenna on Earth, as well as satellite geometry and solar activity. The ionosphere affects code and carrier differently, causing a delay in the code (ionospheric group delay) and an equal and opposite advance in the carrier phase.

The cycle ambiguity is, as described in previous section, the ambiguity on range estimated using the carrier, corresponding to an integer number of carrier cycles. For the purposes of the current work, this ambiguity can be removed by simply removing the data integer mean over lock periods or by high pass filtering the data.

Finally, the last term in Table 2.2 encompasses both receiver noise and multipath. In this work, carrier phase noise is assumed negligible compared to multipath. Therefore, only multipath will be referred to as $\nu_{a(s)}^{k(f)}$ in what follows.

2.4 Dual Antenna (DA) carrier phase multipath characterization

2.4.1 Single and double differences. Since the DA method does not involve any other frequency that $L1$ in this work, the frequency superscript is omitted from the equations in this section, except for the $L1$ wavelength. Note that any other carrier

phase frequency can be used in place of $L1$. Also, if a quantity is not either time, frequency, antenna or frequency dependant, the corresponding sub- or superscript is omitted in the notations. Using the carrier phase measurement model, the single difference of raw carrier phase measurements for satellite s_1 and antennas a_1 and a_2 at time k and for the $L1$ frequency can be written as:

$$\phi^k_{a_1-a_2(s_1)} = r^k_{a_1-a_2(s_1)} + b^k_{a_1-a_2(s_1)} + \lambda^{(L1)} n^k_{a_1-a_2(s_1)} + \nu^k_{a_1-a_2(s_1)} \tag{2.2}$$

The satellite clock biases $\frac{c}{\lambda^{L1}}\delta t^k_{(s_1)}$ (*c.f.* Table 2.2) cancel out at the two receivers a_1 and a_2, since they are solely dependant on the broadcasting satellite s_1. Therefore, only the receiver clock bias difference remains: $b^k_{a_1-a_2(s_1)} = \frac{c}{\lambda^{L1}}(\delta^k_{a_1} - \delta^k_{a_2})$. Adding another satellite – noted s_2 – helps in further cancelling out the undesirable terms. This double difference operation cancels out the receiver clock biases $\frac{c}{\lambda^{(L1)}}\delta t^k_{(a_1)}$ and $\frac{c}{\lambda^{(L1)}}\delta t^k_{(a_2)}$.

$$\phi^k_{a_1-a_2(s_1-s_2)} = r^k_{a_1-a_2(s_1-s_2)} + \lambda^{(L1)} n^k_{a_1-a_2(s_1-s_2)} + \nu^k_{a_1-a_2(s_1-s_2)} \tag{2.3}$$

The term of interest in Equation 2.3 is $\nu^k_{a_1-a_2(s_1-s_2)}$, which contains both thermal noise and multipath error. Thermal noise can be neglected in this case, as mentioned earlier. Note that the result is a combination of multipath from two antennas and two satellites on a single frequency.

From the measurements $\phi^k_{a_1(s_1)}$, $\phi^k_{a_1(s_2)}$, $\phi^k_{a_2(s_1)}$ and $\phi^k_{a_2(s_2)}$, and the known geometric term $r^k_{a_1-a_2(s_1-s_2)}$, the sum of the multipath and cycle ambiguity can be isolated. Then, the ambiguity can be easily removed, by subtracting the mean of the double difference over sequences of continuous tracking of both satellites by both antennas. Finally, these operations leave only the multipath error $\nu^k_{a_1-a_2(s_1-s_2)}$ between the two antennas a_1 and a_2, and from the two satellites s_1 and s_2.

2.5 Dual Frequency (DF) carrier phase multipath characterization

2.5.1 Single difference. The $L1$ minus $L2$ difference can be written:

$$\phi_{a(s)}^{k(L1-L2)} = -I_{a(s)}^{k(L1-L2)} + \lambda^{(L1)} n_{a(s)}^{k(L1)} - \lambda^{(L2)} n_{a(s)}^{k(L2)} + \nu_{a(s)}^{k(L1-L2)} \tag{2.4}$$

The term to be characterized is $\nu_{a(s)}^{k(L1-L2)}$, which is a combination of noise and multipath, with negligible noise, as with the DA method. This time though, the multipath error $\nu_{a(s)}^{k(L1-L2)}$ is a combination of multipath from one antenna, one satellite and two distinct frequencies (in this work, GPS frequencies $L1$ and $L2$). The cycle ambiguity can be dealt with using the same process as with the DA method – removing the mean of the carrier phase data over sequences of continuous tracking of the satellite by the receiver over both $L1$ and $L2$ frequencies. This leaves multipath combined with ionospheric delay, whose removal is discussed in the next subsection.

Note that the current versions of ARAIM use iono-free carrier phase measurements. Since the ionospheric delay is frequency dependent, it can be removed from the carrier phase measurements by using a frequency-scaled version of said carrier phase measurements, yielding an iono-free combination [9]. The multipath observed in ARAIM measurements is therefore an ionospheric delay free version of the multipath error – so it may seem most relevant to derive a multipath model for the iono-free case. However, the iono-free combination contains orbit, clock and tropospheric errors contributions. Instead, in this work, the L1-L2 observable is chosen to derive the multipath error model, because it is free of these additional errors. More explanations are given later on how it relates to multipath in the iono-free combination.

2.6 Ionospheric delay high pass filter cutoff frequency selection

The ionospheric delay from the DF carrier phase single difference in Equation 2.4 can be removed by a high pass filtering operation, since ionospheric delay dynamics occur at a lower frequencies than multipath dynamics. To find a suitable high pass

filter cutoff frequency, the highest frequency of the ionospheric delay dynamics needs to be estimated, which is the focus of this section.

2.6.1 Ionospheric delay model. To have a good approximation of the ionospheric delay at all times and along user-satellite LoS, a model based on the International Reference Ionosphere (IRI) is used. The computation uses the ion densities provided by the IRI-2016 Fortran subroutines [4], fed as input to a custom Matlab routine modified from reference [13]. This custom routine outputs the slant ionospheric delay from zenith ion densities interpolated along the LoS for each satellite in view of a static user. Adapting the simulation for a moving user would not require extensive coding – this will be discussed later in Chapter 5. The relation linking the electron density n_e along the antenna-satellite range $\mathbf{x}_{a(s)}$ to the total electron content (TEC) is stated in Equation 2.5, along with the first order relation linking TEC and ionospheric delay at frequency f. Note that the ionospheric delay approximation is valid for any carrier frequency f. Since it is proportional to the inverse of the frequency squared, for instance given that $L1 > L2$, the $L1$ ionospheric delay will be lower in magnitude than $L2$ ionospheric delay. However, since the TEC factor is the same, ionospheric delay for any frequency will have the same dynamics.

$$I \approx -\frac{40.3 \times \text{TEC}}{f^2}\ [\text{m}] \quad \text{with} \quad \text{TEC} = \int_{\mathbf{x}_{a(s)}} n_e(s)\, ds\ [\text{m}^{-2}] \tag{2.5}$$

The slant ionospheric delay obtained from Equation 2.5 is computed every few seconds for each visible satellite to a given antenna to get precise ionospheric delay profiles along whole satellite passes.

2.6.2 Cutoff frequency selection. To find a suitable cutoff frequency for ionospheric delay removal, the idea is to use ionospheric delay data computed over a large amount of time for a given location using actual GPS satellite position data. However, slant ionospheric delay can only be computed for limited times – during

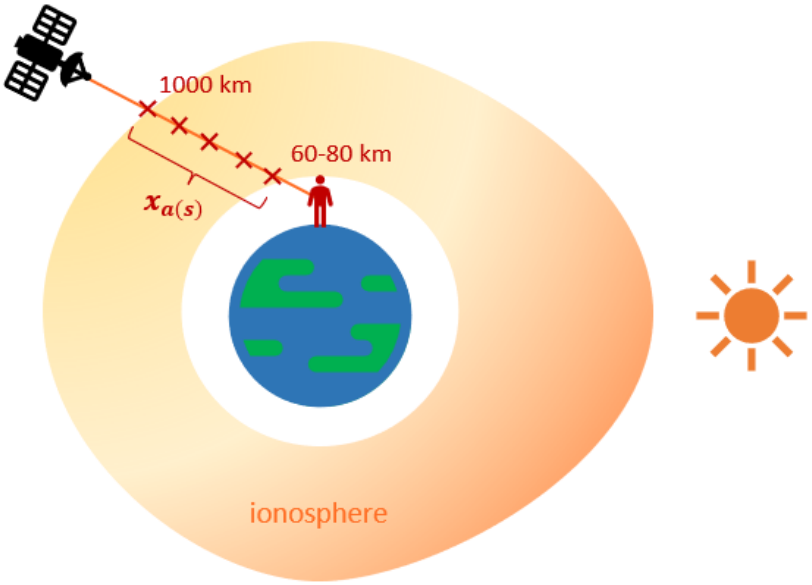

Figure 2.2. Slant ionospheric delay interpolation

satellite passes, when they are in LoS of the reference location. This means that interruptions of a few hours exist in simulated ionospheric delay data sets, making it difficult to estimate the frequency content in the ionospheric dynamics. To help deal with this issue, the cutoff frequency selection method derived in this work uses the Lomb-Scargle (LS) periodogram [14], which is a method for characterizing periodicity in unevenly sampled data. Some more details about the LS power spectral density (PSD) are provided in Chapter 3. The ionospheric delay computed from the IRI model can be considered as unevenly sampled: though ionospheric delay is computed at a set constant rate, the computation can only be done when a satellite is in LoS of the reference location, generating data outages of approximately six hours between passes (*i.e.* from the time a satellite sets to the time it rises again). Using the LS method, an estimate of the ionospheric delay power content for each frequency can be computed. It can be expected that the dominant frequencies will lay at about one and one half sidereal day, which are the GPS constellation repetition period and the orbital period of GPS satellites, respectively. Therefore, only taking the frequency

at the maximum power content as the filter cutoff frequency is not sufficient, as it will leave in a lot of higher frequency ionospheric delay content. Instead, the cutoff frequency f_c is obtained by closely overbounding the LS PSD and computing the minimum frequency for which the power content drops below 40 dB of the maximum power peak, which corresponds to a factor 100 reduction in the time domain. More detail on this process is given in Chapter 4. The time constant τ_c can be retrieved from the highest frequency, f_c, encountered before the 40 dB threshold:

$$f_c = \frac{1}{\tau_c} \tag{2.6}$$

In later occurrences, f_c and τ_c are both used to refer to the ionospheric filter cutoff frequency, though τ_c is usually given in units of minutes, for easier representation. Note that the 40 dB power drop method is a *relative* criterion – meaning it will treat meter level ionospheric delay the same way as it would treat centimeter level delay. A hundredfold decrease for initial decameter level corresponds to a decimeter, while it corresponds to a millimeter for initial meter level. An alternative *absolute* method is also possible. It still relies on a close overbounding of the LS PSD. But with this method, f_c is chosen by integrating the LS PSD model between f_c and the Nyquist frequency f_N until the integral corresponds to a power content of a set value in meters. The integral between f_c and f_N represents the ionospheric delay content that will *not* be filtered out, therefore, it must be negligible with regard to multipath.

Other methods have been considered to find the ionospheric cutoff frequency, such as taking the autocorrelation of each ionospheric delay time series, or fitting a Gauss-Markov Random Process (GMRP) to the power spectral density of ionospheric delay, but since the ionospheric delay data is not stationary, and no known analog to the LS periodogram exists for autocorrelation, these methods have been abandoned.

2.7 Cutoff frequency validation

In this section, a geometric multipath model is developed to justify that the chosen ionospheric delay filter cutoff frequency does not lead to the removal of too much multipath content – as opposed to the method described above, which helps ensure that all (or most) of the ionospheric delay content is removed from the DF carrier phase single difference. Only two multipath reflection scenarios are treated in this work, though a more general case can be considered in future thorough investigations.

2.7.1 Limit case 1: Ground reflections. Assume the GPS antenna to be at an height h above the ground, at a horizontal distance d to the antenna and the GPS signal arrives with an incidence angle θ with respect to the ground in the range $[0, \frac{\pi}{2}]$. Since the satellite sending the GPS signal is far enough away, the direct and reflected signal arrive parallel to each other. Assume the reflections occur following the law of reflection – the incident and reflected signals make the same angle relative to the perpendicular to the surface at the reflection point. The ground reflection situation is schematized on Figure 2.3.

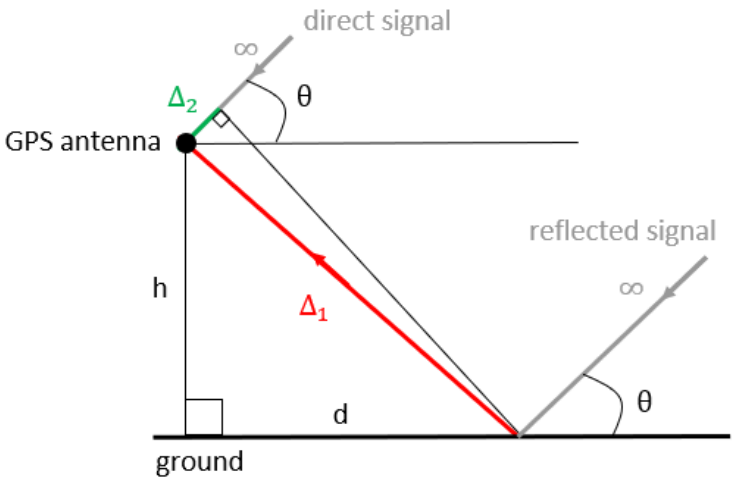

Figure 2.3. GPS signal ground reflection

What has an effect on carrier phase is the extra distance travelled by the signal,

which is, in this case, $\Delta = \Delta_1 - \Delta_2$. By travelling that extra distance, the reflected signal will arrive at the antenna out of phase compared to the direct signal, which has a direct impact on carrier phase measurements. See Appendix A for the derivations (and an alternative model). The resulting extra travelled distance is provided in Equations A.1, A.4 and 2.7:

$$\Delta = 2h \sin\theta \tag{2.7}$$

2.7.2 Limit case 2: Wall reflections. Using the same assumptions as case 1 on the GPS antenna and signal, the wall reflection situation is schematized on Figure 2.4.

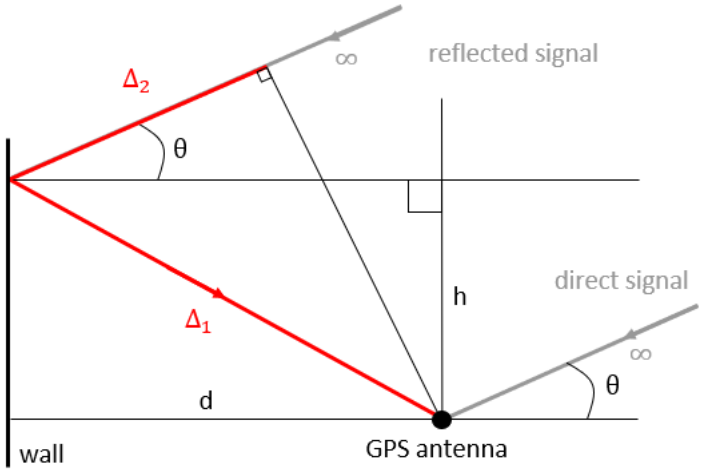

Figure 2.4. GPS signal wall reflection

The signal extra travel distance, $\Delta = \Delta_1 + \Delta_2$ this time, can be found using simple trigonometry and is given in Equation 2.8:

$$\Delta = 2d \cos\theta \tag{2.8}$$

2.7.3 General case. From the two reflection limit cases above, it can be hypothesized that a general reflection case on inclined surfaces can be derived and that this

general case takes the same form, only with a constant phase shift term accounting for the inclination of the surface. This general case will not be treated in this work.

2.7.4 Effects on phase. Consider the results from either of the two cases normalized by λ, the wavelength of the received GPS signal: $\psi = \frac{\Delta}{\lambda}$. The effect of multipath on carrier phase can be described by the quantity $\delta\phi$ as an added contribution to the measured carrier phase ϕ (see Figure 2.5). Figure 2.5 presents the phasor diagram of the sum of both direct and reflected signals – in other words, the actual signal measured at the receiving antenna – assuming a direct signal amplitude of 1 and a reflected signal amplitude of α. The relationship in Equation 2.9, linking the extra travelled distance by the reflected signal, the geometry of the reflection environment and the contribution to the carrier phase can then be derived.

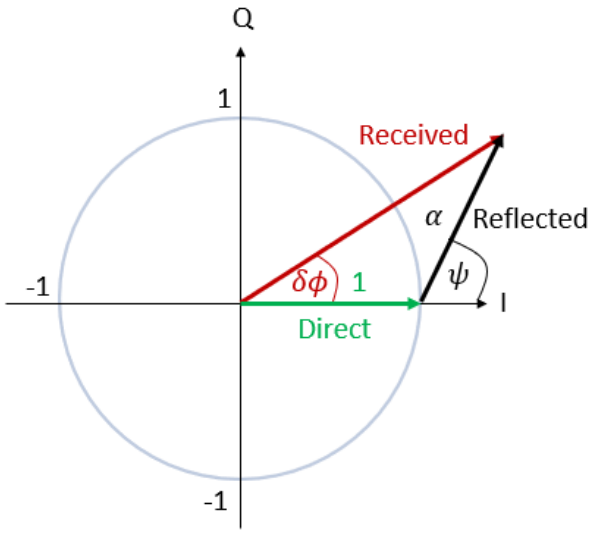

Figure 2.5. Direct and reflected signals contribution to carrier phase

$$\tan \delta\phi = \frac{\alpha \sin \psi}{1 + \alpha \cos \psi} \tag{2.9}$$

From here on, two situations will be investigated. Mathematically, case 1 is if $\alpha << 1$, and case 2 if $\alpha < 1$ but not $\alpha << 1$. No extra cases are needed since the reflected signal amplitude will nearly always be less than the direct – due both

to partial absorption of the signal by the reflector as well as low antenna gains for signals arriving from low (including negative) elevations.

If $\alpha << 1$ (case 1) – *i.e.*, if the reflected signal has a very small magnitude relative to the direct signal – then $\tan\delta\phi \approx \delta\phi \approx \alpha\sin\psi$, which translates to Equation 2.10 for ground and for wall reflections, with $z = \frac{2d}{\lambda}$ in the wall reflection case, and $z = \frac{2h}{\lambda}$ in the ground reflection case.

$$\begin{cases} \delta\phi \approx \alpha\sin(z\cos\theta) \\ \delta\phi \approx \alpha\sin(z\sin\theta) \end{cases} \tag{2.10}$$

Equation 2.10 can be expanded using the Jacobi-Anger expansion presented in Equation 2.11 [15], into the expressions stated in Equation 2.12.

$$\forall x, y \in \mathbb{R}^2, \begin{cases} \sin(x\cos y) = -2\sum_{n=1}^{+\infty}(-1)^n J_{2n-1}(x)\cos((2n-1)y) \\ \sin(x\sin y) = 2\sum_{n=1}^{+\infty} J_{2n-1}(x)\sin((2n-1)y) \end{cases} \tag{2.11}$$

where J_n is the n^{th} Bessel function of the 1^{st} kind. In a given (z, θ) geometric situation, this yields:

$$\begin{cases} \delta\phi \approx \alpha\sin(z\cos\theta) = -2\alpha\sum_{n=1}^{+\infty}(-1)^n J_{2n-1}(z)\cos((2n-1)\theta) \\ \delta\phi \approx \alpha\sin(z\sin\theta) = 2\alpha\sum_{n=1}^{+\infty} J_{2n-1}(z)\sin((2n-1)\theta) \end{cases} \tag{2.12}$$

If $\alpha < 1$ but not $\alpha << 1$ (case 2), let us use the truncated Taylor series approximation for $x \mapsto \frac{1}{1+x}$ on Equation 2.9. This yields Equation 2.13.

$$\tan\delta\phi = \frac{\alpha\sin\psi}{1+\alpha\cos\psi} = \alpha\sin\psi \times (1 - \alpha\cos\psi + \mathcal{O}(\alpha^2)) \tag{2.13}$$

To further simplify Equation 2.13, the truncated Taylor series approximation for $x \mapsto \tan x$ is used, leading to Equation 2.14.

$$\delta\phi + \mathcal{O}(\delta\phi^2) = \alpha\sin\psi \times (1 - \alpha\cos\psi + \mathcal{O}(\alpha^2)) \tag{2.14}$$

Simplifying Equation 2.14, and dropping terms of order 3 and higher yields Equation 2.15.

$$\delta\phi \approx \alpha \sin\psi \times (1 - \alpha\cos\psi) = \alpha\sin\psi - \frac{\alpha^2}{2}\sin 2\psi \tag{2.15}$$

This expression can also be expanded using the Jacobi-Anger expansion, Equation 2.11, which yields the expansion in Equation 2.16 for the carrier phase multipath $\delta\phi$ in this second case.

$$\begin{cases} \delta\phi \approx \alpha \sum_{n=1}^{+\infty} (2J_{2n-1}(z) - \alpha J_{2n-1}(2z))(-1)^n \cos((2n-1)\theta)) \\ \delta\phi \approx \alpha \sum_{n=1}^{+\infty} (2J_{2n-1}(z) - \alpha J_{2n-1}(2z)) \sin((2n-1)\theta)) \end{cases} \tag{2.16}$$

Note that for both cases (Equations 2.12 and 2.16), the carrier phase multipath amplitudes are determined by the Bessel functions $2J_{2n-1}(z)$ and $2J_{2n-1}(z) - \alpha J_{2n-1}(2z)$ (first order only and first and second order contributions), respectively. By studying the main terms of each expansion, for a given geometric configuration (z, θ), one can determine the multipath power content above and below f_c, a candidate filter cutoff frequency. This is done by scaling the integer term $2n-1$ to the frequency domain, using the frequency at which the geometric situation (z, θ) changes. In the rooftop case presented in Chapter 4, for instance, the geometric situation changes at the rate of change of the GPS satellites position, which is half a sidereal day. In the airplane case presented in Chapter 5, other frequencies result in a geometric situation periodic change: airplane in-flight dynamic modes. More details and results are given in the relevant Chapters. As mentioned previously, the power content below the cutoff frequency of the ionospheric delay filter f_c is largely removed by the filtering operation. If this power content is negligible relative to the total multipath power content estimated using the Jacobi-Anger expansion, then f_c can be validated.

CHAPTER 3
FREQUENCY-DOMAIN BOUNDING

To use GNSS data in an INS/GNSS integrated system that relies on a KF – which is common practice – one needs to have at least some knowledge of the variances of the errors involved. The PSD approach chosen here however, does even more than that: it estimates and bounds the stochastic dynamics of the errors, not just their variances. This property makes a strong case for the use of this method in KF ARAIM, which requires error models over time, and not just snapshot models only valid at one instant in time. The idea is to take the PSD – which is formally defined later in this Chapter – of an error signal, then find a simple first order GMRP based model that strictly upper bounds it [6]. From the derivations presented in the following sections, using an upper bound on the PSD in a KF algorithm is a sufficient condition to obtain an upper bound on the KF state estimate error variances.

3.1 Power Spectral Density (PSD)

The PSD S_{XX} of a zero-mean, stationary process is defined as the Fourier transform of the autocorrelation function (ACF) R_X of a time-dependant signal x, or X in the frequency domain. Equation 3.1 defines the PSD from the ACF. In reality, this is a result from the Wiener-Khinchin theorem for wide sense stationary processes [16].

$$\forall \omega \in \mathbb{R}^+,\ S_{XX}(\omega) = \int_{-\infty}^{+\infty} R_X(t) e^{-j\omega t}\, dt \tag{3.1}$$

Reference [17] showed that an upper bound in the PSD domain automatically results on an upper bound in the variance domain. Mathematically:

$$S_{XX} < \overline{S_{XX}} \Rightarrow \sigma_y < \overline{\sigma_y} \tag{3.2}$$

Equation 3.2 was shown in [17] for the stationary input case only, but can be extended to other cases as well – all of which are given in the bullet points below. The proof for each case will be the topic of an upcoming paper by the Navigation Laboratory at Illinois Institute of Technology, and based on [18].

- Steady state KF with stationary input
- Time-varying KF with stationary input
- Time-varying KF with non stationary input with slowly changing non stationarity

A fourth case is time-varying KF with non stationary input and quickly changing non stationarity. In practice, it should not be encountered with aircraft multipath, since the associated KF time constant would likely be of the order of the minute, while the non stationarity changes would likely be of the order an hour, since it evolves with satellite elevation (more on this later). However, the fourth case would most certainly be encountered when considering multipath in cluttered (*e.g.* dense urban zones) areas, especially in a very dynamic environment (*e.g.* close to high traffic areas) where reflection sources are diverse, plentiful, and ever-changing.

3.2 Stationarity analysis

As will be seen later (Chapter 4), multipath is satellite elevation dependent. Therefore, carrier phase multipath data will almost never be stationary since the variance of the data increases as the elevation of its satellite decreases. To alleviate this issue, a deterministic normalizing function is applied to the data in order to remove the elevation dependency:

$$M : \phi_{a(s)}^{k(L1-L2)} \mapsto \frac{\phi_{a(s)}^{k(L1-L2)}}{a + be^{-\frac{(\mathrm{el}(s)^k)^2}{2}}} \tag{3.3}$$

The term $\mathrm{el}(s)^k$ designates the elevation of the satellite s at time k.

After normalization, two stationarity tests are performed to ensure that all sample data sets are stationary:

- **Levene test** [19] – Assesses the equality of variances between sample sets. This test is used on samples sets split in 4.
- **2-samples Kolmogorov-Smirnov (K-S) test** [20] – Assesses whether two sample sets come from the same distribution. This test is used on sample sets split in 2.

Theoretically, the stronger test is the K-S test, since it compares cumulative distribution directly, so it could be used by itself, but it is also the more computationally heavy to run. Therefore, the sample sets are first subjected to the Levene test. If they are deemed non stationary by the Levene test, there is no need to run the K-S test. If the samples are deemed stationary in the Levene sense, however, the 2-sample K-S test is run to ensure stationarity.

3.3 PSD upper-bounding model

The PSD model used for upper bounding carrier phase multipath error is a combination of a first order GMRP with standard deviation σ_{GM} and time constant τ_{GM} and Gaussian white noise N_{WN} with variance σ_{WN} [6], expressed in Equation 3.6. The ACF of a first order GMRP with time constant τ_{GM} and standard deviation σ_{GM} is expressed in Equation 3.4 [21]. The ACF of white noise with standard deviation $\sigma_{WN} = \sqrt{R_{WN}(0)}$ is expressed in Equation 3.5, with δ the Dirac function.

$$R_{GM} : t \mapsto \sigma_{GM}^2 e^{-\frac{t}{\tau_{GM}}} \tag{3.4}$$

$$R_{WN} : t \mapsto N_{WN}\delta(t) \tag{3.5}$$

$$S_{XX} : f \mapsto \frac{\frac{2\sigma_{GM}^2}{\tau_{GM}}}{\frac{1}{\tau_{GM}^2} + 4\pi^2 f^2} + N_{WN} \tag{3.6}$$

The selectable bounding parameters for this model are σ_{GM}, τ_{GM} (the first order GMRP parameters), and σ_{WN} (the white noise variance).

3.4 Lomb-Scargle PSD estimate

The Lomb-Scargle (LS) periodogram [14] and PSD estimate, introduced in Chapter 2, can also be of use in the design of a PSD upper bounding model. The chosen approach for the DF method in this work is to filter out the ionospheric delay from the DF single difference. In theory, the filtering operation can be done either before or after taking the PSD of the data – both options are mathematically correct, and have their advantages and drawbacks, which are summed up in Table 3.1.

Table 3.1. Advantages and drawbacks of filtering in the time and frequency domains

	Time domain filtering	**Frequency domain filtering**
Advantages	Use of classic PSD	Multiplication-based filtering
	Same PSD as in [6] and [5]	Same LS PSD as in cutoff frequency determination
Drawbacks	Filtering artifacts on the PSD depending on filter used	LS PSD not as precise as PSD for evenly sampled data
	Convolution based filtering	Need longer data sequences for ensuring accuracy

A very strong argument for sticking with the filtering in the time domain is the argument of harmonicity with references [6] and [5], who define error models based on the classic definition of PSD. But the frequency domain method can be a tool to verify that the ionospheric delay is removed correctly, and that the IRI model used to compute the ionospheric delay described in Chapter 2 does indeed reflect the real dynamics of the ionosphere. Therefore, though it is recommended to use the classic

PSD and filtering in the time domain for a final result, the LS periodogram and PSD can be used for "safety checks". Note that the LS PSD results can only help verify the accuracy of the ionospheric cutoff frequency on the ionospheric delay side. It is still recommended to use the Bessel function-based Jacobi-Anger expansion presented in Chapter 2 to ensure that the chosen cutoff frequency does not remove too much multipath content during the filtering step.

CHAPTER 4

ROOFTOP DATA EXPERIMENT

A rooftop antenna experiment was performed as a benchmark test case for the DA and DF methods in preparation for future application to actual aircraft data. This Chapter provides the practical details of and results from the implementations of the DA and DF methods.

4.1 Data collection

The GPS data used for DA and DF multipath characterization in this Chapter was collected using two antennas placed on the rooftop of Illinois Institute of Technology Rettaliata Engineering Center building in Chicago, IL. The data collection was performed on November 24, 2020, and lasted for 24 hours, with a sample rate of 1 second. From the GPS data, only GPS time, satellite orbit information, and carrier phases from the $L1$ and $L2$ frequencies are used.

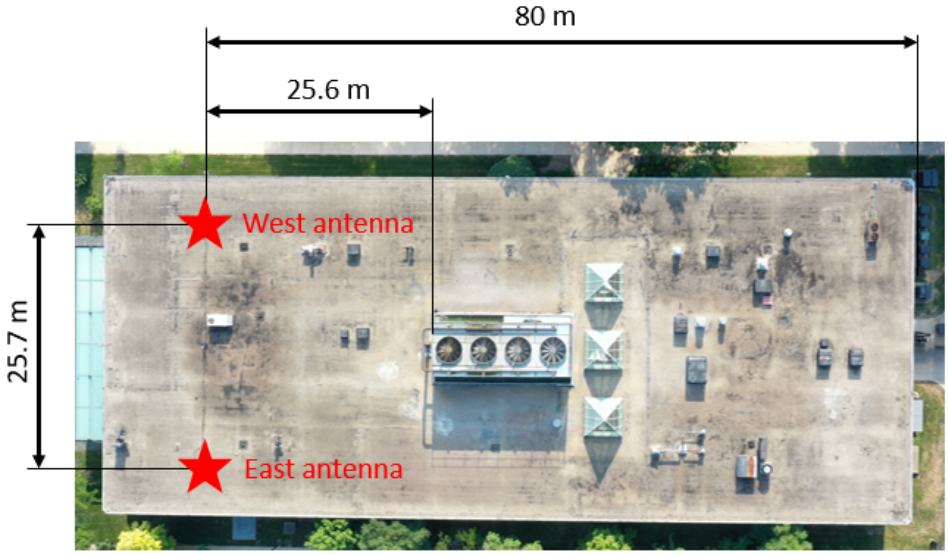

Figure 4.1. Rooftop antennas placement

The latitude and longitude in units of decimal degrees of the data collection are $(\text{lat}, \text{lon}) = (41.84°, -87.63°)$. The antennas are placed on the rooftop as shown in Figure 4.1. The distances pictured are approximate, and will be relevant later, during the ionospheric delay filter cutoff frequency verification step.

4.2 Dual Antenna (DA) carrier phase multipath characterization

4.2.1 Data matching. The first step to prepare raw carrier phase measurements for DA multipath characterization and bounding is data matching. In this step, only carrier phase data that is available from two satellites of interest and collected on both rooftop antennas simultaneously is kept. A visualization of the GPS seconds at which healthy satellites from PRN 1 to 32 were in LoS and provided $L1$ carrier phase measurements to both rooftop antennas on November 24, 2020 is shown on Figure 4.2.

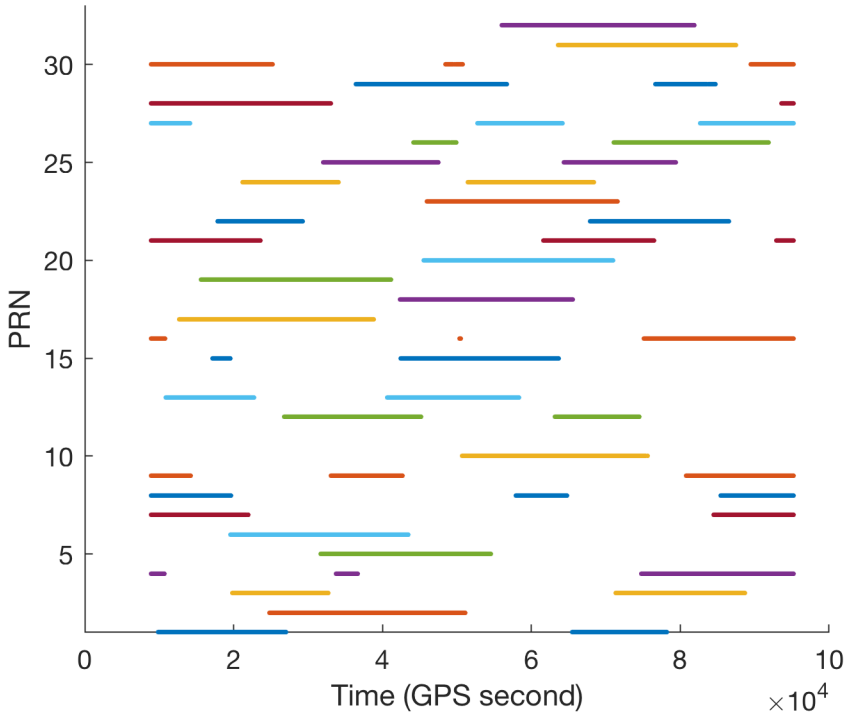

Figure 4.2. LoS satellites on Nov. 24 2020 (GPS week 2132)

According to Figure 4.2, PRN 20 and 23 are in LoS of both rooftop antennas at roughly the same time during the day of data collection. Results from these two PRN are used as reference cases for the DA method results presented here.

4.2.2 Single and double differences. From the matched data, the single and double differences can be performed. The single difference consists in subtracting carrier phase measurements from a single satellite across the two rooftop antennas. This is shown for two distinct PRN (20 and 23), but done for multiple PRN pairs, so that there are more that one double difference for PSD overbounding. Those two resulting carrier phase single differences are then differenced from each other – resulting in the double difference. Then, this double difference is cleaned, meaning lock periods (*i.e.* sequences over which the receiver locks on a certain GNSS satellite) that last less that a predefined length threshold are removed from the single difference dataset. The minimal length threshold used for this work is 30 minutes – which means only data from satellites that have been tracked continuously by a receiver for more than 30 consecutive minutes are considered. This thresholding on the length of time series is also performed for the DF method. Finally, as discussed in section 2.4, the known range term is removed as is the integer mean of the double differenced carrier phase measurements over the remaining lock periods (to eliminate the cycle ambiguity). Figure 4.3 presents the results from the double difference for PRN 20 and 23 (raw and mapped according to Equation 3.3). From inspecting the raw estimated DA carrier phase multipath (dark blue on Figure 4.3), it is clear that DA multipath is elevation dependant – as the multipath error value at the start and end of the data, where the satellites are at low elevations, is larger than in the middle of the data, where the satellites are at their higher elevations. The chosen mapping function parameters (*c.f.*, Equation 3.3) are $a = 1$, $b = 29$ and $c = 10$. Note that the mapping function uses the elevation from only one satellite. In the DF case, to be discussed later, only one satellite is considered – it is therefore evident which elevation to use.

However, in the DA case, carrier phase measurement from two distinct satellites are collected. The mapping function therefore becomes satellite-dependent, with $k \in [\![k_1, k_2]\!]$, $\text{el}(s)^k = \min(\text{el}(s_1)^k, \text{el}(s_2)^k)$ with k_1 and k_2 the start and end time of the data matched sequences.

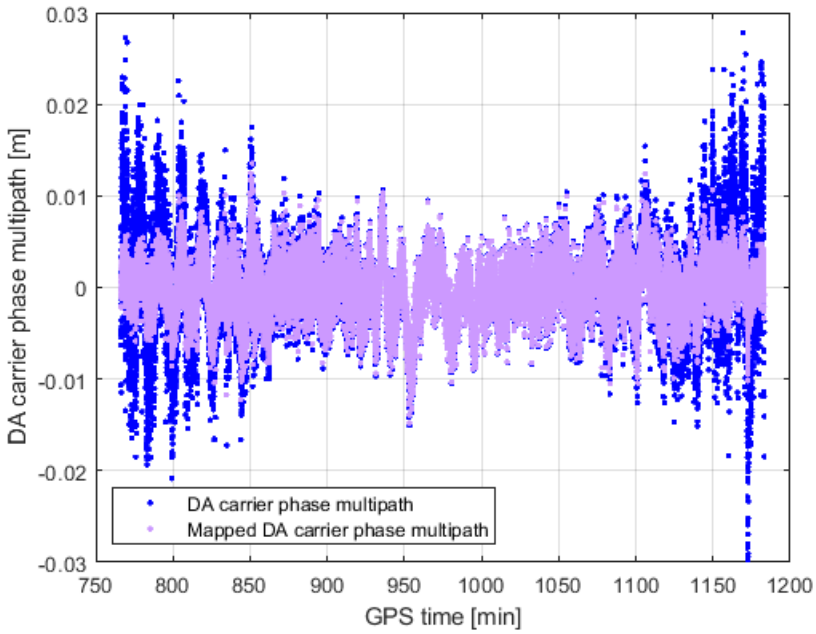

Figure 4.3. Raw and mapped DA carrier phase multipath – PRN 20-23

4.2.3 Stationarity analysis. On the mapped carrier phase multipath samples, the Levene test is run first, since it is the weaker and the least computationally heavy stationary test of the two presented in Chapter 3. If the sample is deemed non stationary from the Levene test, then it is trimmed until deemed stationary in the Levene sense, using a custom windowing algorithm described in the next section. If the sample turns out stationary, then the stronger 2-samples K-S test is run, and the same process is repeated: a non stationary sample is trimmed until stationary, and rejected if the minimum acceptable sample length is reached and the sample still does not test as stationary. The full windowing algorithm for stationarity analysis is described in detail in the next subsection.

4.2.4 Windowing. Let us define a sample set as a sequence of data collected continuously from GNSS lock acquisition to loss of lock, and a sub-sample any sub-sequence included in or equal to a given sample. The windowing algorithm can be summed up in the block diagram in Figure 4.4. The notations used are defined in Table 4.1. Note that the expressions in bold font evaluate to Boolean, and their negation is represented with an overlying bar.

Table 4.1. Windowing algorithm notations

Notation	Definition
i_{st}	Index of start of sequence in given sample set
i_{sp}	Index of end of sequence in given sample set
$w_{st,k}$	Index of start of window in given sample at step k
$w_{sp,k}$	Index of end of window in given sample at step k
L	Smallest acceptable sub-sample length
$\boldsymbol{s_k}$	StationarityTest(data($w_{st,k} : w_{sp,k}$))
$\boldsymbol{l_{s,k}}$	$i_{sp} - \lfloor p_{slide} w_{k,st} \rfloor + 1 \geq L$
$\boldsymbol{l_{t,k}}$	$\lfloor p_{trim} w_{sp,k} \rfloor - w_{k,st} + 1 \geq L$
$\boldsymbol{e_k}$	$w_{sp,k} = i_{sp}$

The entire initial sample is tested for stationarity first, with start and stop indexes i_{st} and i_{sp} respectively. Hence, the window indexes are initialized such that $w_{st,0} = i_{st}$ and $w_{sp,0} = i_{sp}$. Then, the stationarity tests are run – first, the Levene test. A negative Levene test outcome sets the value of the stationarity flag to $\boldsymbol{s_k} = 0$. A positive Levene test outcome triggers the 2-sample K-S test – a positive outcome from this second test sets $\boldsymbol{s_k} = 1$ and a negative outcome sets this flag to 0. The

next action is decided by the value of the Booleans $\boldsymbol{s_k}$, $\boldsymbol{l_{t,k}}$ and $\boldsymbol{l_{s,k}}$. If the sample is deemed stationary, then the window indices are stored, to keep track of where in the data to look for for a stationary sub-sample. Then, there are two possible outcomes, depending on the value of $\boldsymbol{l_{s,k}}$ and $\boldsymbol{e_k}$:

- **Slide** the window if $\overline{\boldsymbol{e_k}}$ & $\boldsymbol{l_{s,k}}$ – *i.e.*, if the end of the sample set is not reached ($w_{sp,k} \neq i_{sp}$) and if the new sub-sample length after sliding falls above the threshold length L

- **End** the algorithm if $\boldsymbol{e_k}$ | ($\overline{\boldsymbol{e_k}}$ & $\overline{\boldsymbol{l_{s,k}}}$) – *i.e.*, if the end of the sample set is reached, or if it is not reached but the new sub-sample length after sliding is shorter than the minimum acceptable length L

If the current sub-sample is deemed nonstationary, however, the window indices are not stored. From here, there are three possible actions that depend on the current stop index of the window, the potential length after trimming and the potential length after sliding the window:

- **Trim** the window if $\boldsymbol{l_{t,k}}$ – *i.e.*, if the new sub-sample length after trimming is above L

- **Slide** the window if $\overline{\boldsymbol{l_{t,k}}}$ & $\overline{\boldsymbol{e_k}}$ & $\boldsymbol{l_{s,k}}$ – *i.e.*, if the new sub-sample length after trimming is below L, but the sub-sample length after a potential sliding action is above L and the end of the sample is not reached

- **End** the algorithm if $\overline{\boldsymbol{l_{t,k}}}$ & ($\boldsymbol{e_k}$ | $\overline{\boldsymbol{e_k}}$ & $\overline{\boldsymbol{l_{s,k}}}$) – *i.e.*, if neither trimming nor sliding the current sub-sample is acceptable even though the end of the sample is not reached, or if the end of the sample is reached

From this point on, the new sub-sample defined by $w_{st,k+1}$ and $w_{sp,k+1}$ is tested for stationarity – and the whole process is repeated until an endpoint is reached. The whole windowing process is summed up on Figure 4.4.

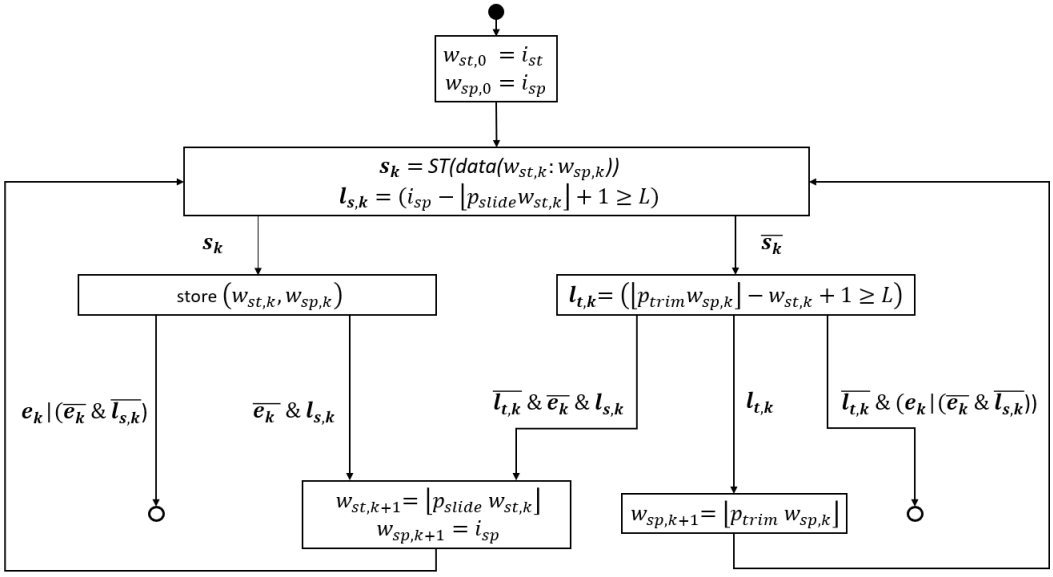

Figure 4.4. Windowing algorithm flowchart

This algorithm conveniently adapts to "less stationary" data, in the sense that if the underlying dynamics change faster than usual in some sections of a sample, the windows to check for stationarity will be smaller in those sections, maximizing the number of potentially stationary sub-samples. The values of p_{slide} and p_{trim} can be chosen at will depending on how much overlapping is desired. These sliding and trimming coefficients are somewhat adaptive, since they depend on the current window size. This adaptiveness avoids generating too much sub-sample overlapping, especially in the case of smaller windows. In this work, $p_{slide} = 1.2$ and $p_{trim} = 0.8$, represent a percentage of the current windowing index. One noteworthy point is this algorithm does not guarantee full coverage of the initial sample, in the sense that there can be sections of data that are not stationary at all however small the window – see Figure 4.5, case (b). This would be observed when trying to split highly nonstationary data into stationary bits – *i.e.*, when in presence of outlier sequences.

This is not a common occurrence, and could be accounted for in future work. Figure 4.5 provides a visual representation of windowed data – in the nominal case (a), and when in presence of an outlier sequence (b). The figure is not based on the real windowing obtained from the data sequences – it is a simplified example.

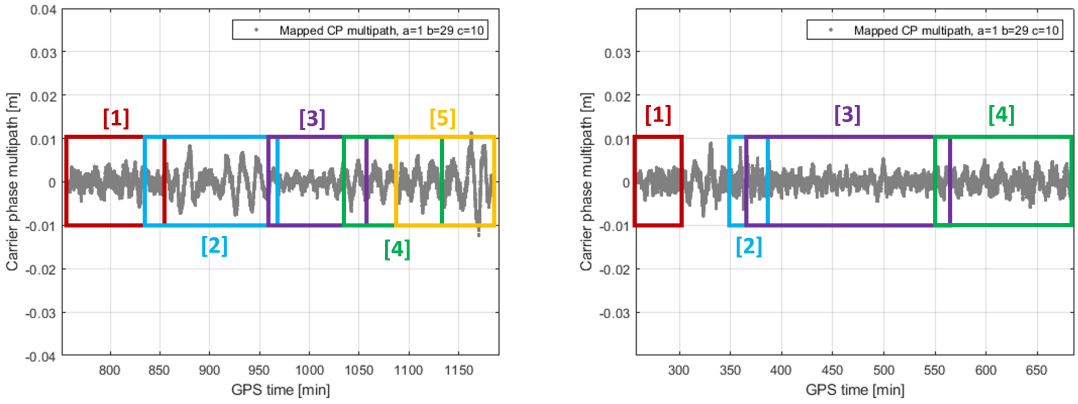

(a) Full coverage windowing

(b) Windowing with outlier sequence

Figure 4.5. Stationarity based windowed data example

4.2.5 Frequency-domain bounding. After mapping the DA carrier phase multipath error data and submitting it to the stationarity tests and windowing as described in the previous two subsections, the PSD can be computed and the upper bound designed, as can be seen on Figure 4.6. To avoid redundancy in detailing the procedures, all mapping, stationarity testing and windowing related information is presented in this section on DA only, but are also used (cited where relevant) for the DF multipath characterization method and PSD bounding, which is the main focus of this work.

As stated in Chapter 3, the PSD is computed from the Fourier transform of the ACF of the data (see Equation 3.1). For this, a smoothed rectangular tapering window is used. This window is adaptive to the length of each data time sequence. It uses 80 % of the data, and slowly damps out the remaining 20 %. This is mostly to reduce the spectral leakage phenomenon. Figure 4.6 presents the results for the

PSD bounding of each stationary mapped (and scaled according to Appendix B) DA carrier phase window.

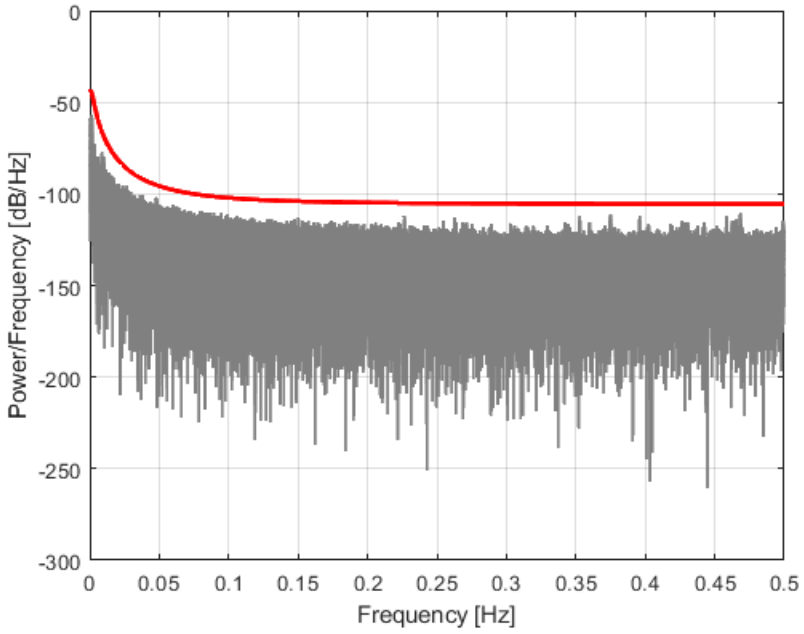

Figure 4.6. DA PSD bounded carrier phase multipath and GMRP upper bound

The selected bounding parameters, as presented in Chapter 3, are the following:

$$\begin{cases} \sigma_{GM}^{(DA)} = 0.5\text{cm} \\ \tau_{GM}^{(DA)} = 45\text{s} \\ \sigma_{WN}^{(DA)} = 0.2\text{cm} \end{cases} \tag{4.1}$$

This model does seem close to what was to be anticipated for DA carrier phase multipath, since the expected time constant and variance for multipath are of about 30 s and 1 cm respectively. However, in this DA rooftop experiment, measurements from two antennas in a short baseline configuration are used. Since the two antennas *see* roughly the same environment, it can be assumed that some of the multipath error is cancelled out when taking the single difference. That is why this model might not be completely representative of what a single antenna user will experience, and

$\sigma_{GM}^{(DF)}$ and $\sigma_{WN}^{(DF)}$ can be expected to be slightly different (probably larger) in the DF case than $\sigma_{GM}^{(DA)}$ and $\sigma_{GM}^{(DA)}$ respectively for the DA case. $\tau_{GM}^{(DF)}$ should be roughly the same value as $\tau_{GM}^{(DA)}$.

4.3 Dual Frequency (DF) carrier phase multipath characterization

4.3.1 Data matching. The first step in the DF multipath characterization method is also data matching – but it is not the exact same step performed for the DA method. In this case, measurements from two distinct frequencies collected simultaneously at the same antenna are kept.

4.3.2 Single difference. From the matched $L1$ and $L2$ raw carrier phase measurements, the single difference can be computed. As stated in Chapter 2, the single difference is a composite of DF multipath, ionospheric delay and cycle ambiguity. The last two contributions are removed by a high pass filtering operation, since the cycle ambiguity is a constant term (zero-frequency). However, the cycle ambiguity can also be removed before filtering by removing the integer mean – it has theoretically no influence on the results. At this point, the 30 minute thresholding on the length of the data time sequences is performed, as described in the previous section.

Figure 4.7 shows the DF single difference before ionospheric delay removal. The slow frequency phenomenon is ionospheric delay. By zooming in on the data points, a higher frequency phenomenon can be seen – DF carrier phase multipath. Those two phenomenon are visually of very different frequencies – that is why they can be separated using a filtering operation. The next subsection focuses on computing a suitable high pass filter cutoff frequency f_c for ionospheric delay removal for the rooftop benchmark case.

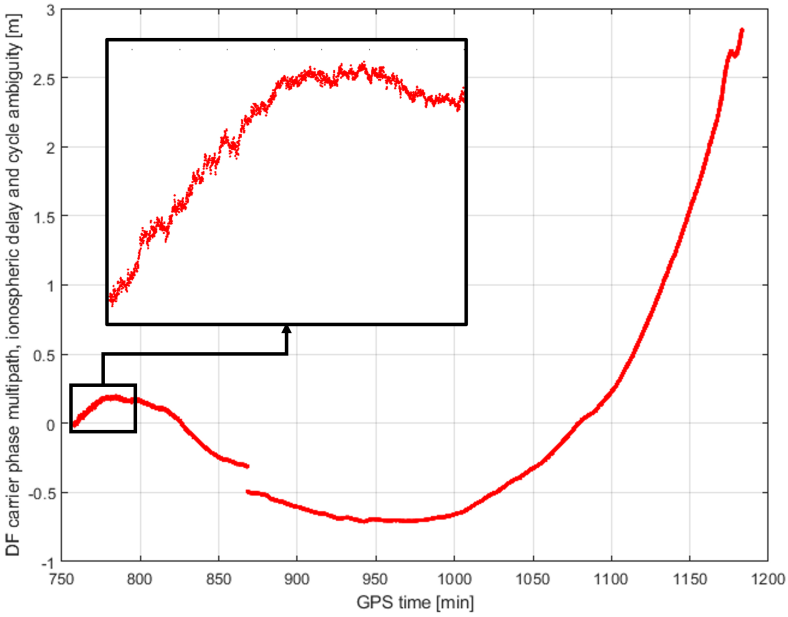

Figure 4.7. DF mutipath, ionospheric delay and cycle ambiguity – PRN 20

4.3.3 Ionospheric delay removal by high pass filtering. As described in Chapter 2, the ionospheric delay error present after the DF single difference is removed using a high pass filter. For this filter, the cutoff frequency f_c needs to be determined, using local ionospheric delay dynamics information. To get an accurate ionospheric delay representation, the IRI model is run for each Monday of the first full week of each month for one year, at the Chicago location coordinates stated in the first section of this Chapter 4, and for each healthy satellite in LoS. From these computed ionospheric delays, the method followed to estimate the filter cutoff frequency is:

1. **Replicate the ionospheric delay data over multiple days** – To ensure that the natural frequencies of the ionospheric delay dynamics are estimated properly, and since the LS periodogram is based on sinusoidal fits at each frequency, the more cycles available the better. Figure 4.8 shows the one-day ionospheric delay computed based on the IRI model (left plot) and the seven-days replicated ionospheric delay (right plot). Since the ionospheric delay is computed using

GPS satellite position and the GPS constellation has a ground-track repetition period of one sidereal day ($\approx$ 23 h 56 min 4 s), the data is replicated in sidereal day intervals.

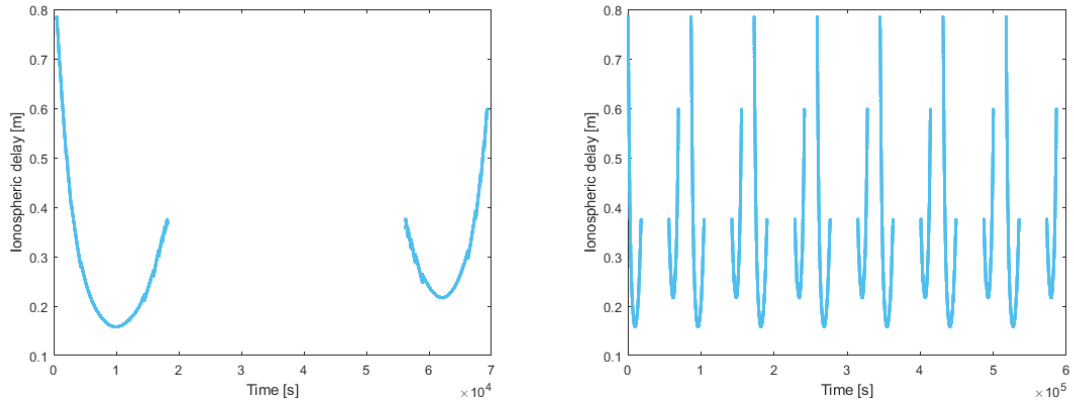

(a) Single day

(b) 7 days replication

Figure 4.8. Ionospheric delay – PRN 1, January 5 2020

2. **Compute the LS PSD of the replicated data** – *c.f.*, Figures 4.9 and 4.10 (left plots) show the LS PSD of the ionospheric delay repeated over seven days for January 5, 2020 and PRN 1 and for each simulation day and all PRN, respectively.

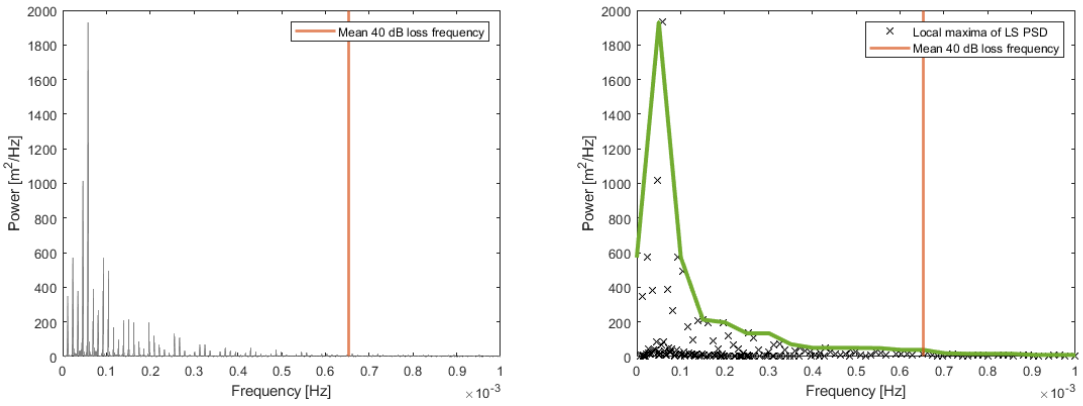

(a) LS PSD

(b) LS PSD local maxima quantile regression

Figure 4.9. LS PSD and quantile regression – PRN 1, January 5 2020

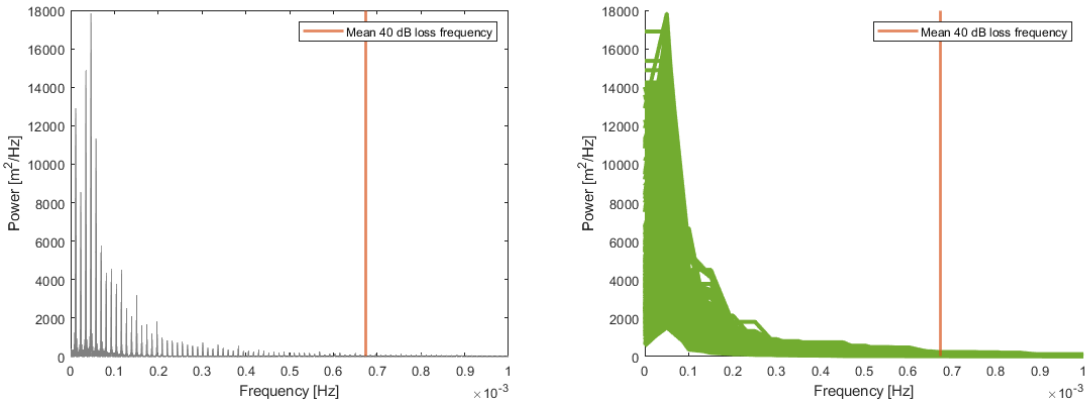

(a) LS PSD

(b) LS PSD local maxima quantile regression

Figure 4.10. LS PSD and quantile regression – all PRN, year 2020

3. **Estimate the upper bound of local maxima of the PSD using quantile regression** – To find where the power globally drops below 40 dB, a close upper bound of the local maxima of the PSD is needed – since some frequencies in between the large power peaks may have power content below this 40 dB drop threshold. To do this, a 100% quantile regression is used. The result of this quantile regression is a curve that links all highest local maxima. From there, the frequency at which the curve drops below the maximal power peak value minus 40 dB, and stays under this threshold, can be chosen as f_c. Figure 4.9 (right plot) shows all the local maxima of the LS PSD for January 5, 2020 (black crosses), and the resulting bounding curve (green curve). Figure 4.10 (right plot) shows the LS PSD upper bound for each simulation day and all PRN.

4. **Find the frequency f_c at which the PSD drops below 40 dB of the maximum power** – A 40 dB drop in the power domain corresponds to a factor 100 reduction in amplitude. Figures 4.9 and 4.10 show the mean f_c for the year 2020, but the f_c chosen as the cutoff frequency for the ionospheric delay filter is the maximum f_c encountered. This ensures that when using this cutoff

frequency on the carrier phase data, little to no ionospheric delay remains after the filtering step.

This algorithm is repeated on the ionospheric delay computed for each day and each PRN in LoS at the Chicago location – *i.e.*, on approximately 350 data files. The mean, maximal and minimal f_c are, respectively: 6.73×10^{-4} Hz, 9.55×10^{-4} Hz and 5.03×10^{-4} Hz – which corresponds, in units of minutes, to time constants 24.76 min, 17.46 min and 33.17 min. Equation 4.2 states the chosen cutoff frequency – which is the maximal frequency encountered, because it corresponds to the maximal ionospheric delay natural frequency encountered for the whole year 2020 (assuming no anomalous events impacted the ionospheric layer). Meaning, during the year 2020, no substantial higher frequency content has been encountered in ionospheric delay dynamics. This cutoff frequency will therefore remove most of the ionospheric delay content present in the DF carrier phase single difference.

$$f_c = 9.55 \times 10^{-4} \text{ Hz} \Leftrightarrow \tau_c = 17.46 \text{ min} \tag{4.2}$$

To be certain the cutoff frequency in Equation 4.2 does not remove too much multipath content along with ionospheric delay, let us use the Jacobi-Anger expansion presented in Equation 2.16, and explained in Chapter 2. As can be seen in Figure 4.11, whatever frequency content is to the right of the vertical line (representing the cutoff frequency of the high pass filter) is conserved in the filtering process, and whatever is to the left is damped or completely removed. The Jacobi-Anger expansion described in Chapter 2 is used here to estimate the carrier phase multipath power in the frequency domain to see if the selected ionospheric delay cutoff frequency will remove negligible (or not) carrier phase multipath content. Figure 4.11 is a representation of the predicted carrier phase multipath power – in red on Figure 4.11, $(2J_{2n-1})^2$ and in black $(2J_{2n-1}(z) - \alpha J_{2n-1}(2z))^2$, such that frequencies lie in $[\![0, f_N]\!]$,

where $f_N = \frac{1}{24}$ is the Nyquist frequency (ionospheric delay data is computed every 12 seconds). z is taken to be $\frac{50}{\lambda^{(L1)}}$ (*c.f.*, Chapter 2 and Section 4.1) with $d = 25$ m approximately corresponding to the horizontal distance of the reflection point on the closest obstacle (wall reflection case). Note that Figure 4.11 also shows that there is minimal difference between the first order only (when $\alpha << 1$, *c.f.* Chapter 2) and the first and second order (when $\alpha < 1$ but not negligible with regard to 1, *c.f.* Chapter 2) expansions. Therefore, the first order expansion is sufficient to verify f_c for all cases.

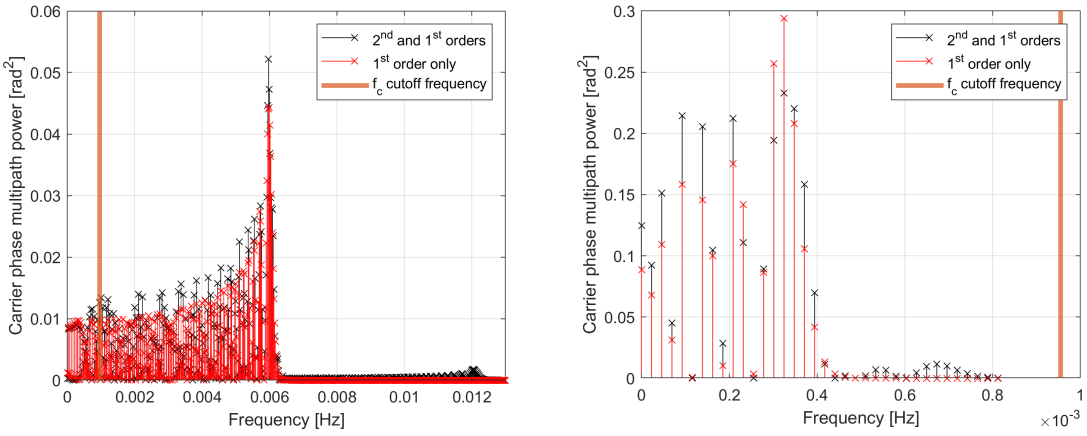

(a) Wall reflections

(b) Ground reflections

Figure 4.11. f_c validation through Jacobi-Anger expansion (rooftop benchmark case)

In Figure 4.11, the plot of the Jacobi-Anger expansions (Equations 2.12 and 2.16) for the rooftop wall reflection case (a), what is removed or damped by the filter corresponds to a small percentage of the carrier phase multipath total power ($< 10\%$), even with the reflection geometry changing at the slow rate of the GPS satellite ground-track repetition period. However, when considering the ground reflection case (b), with the antenna being at an height of approximately $h = 1.5$ m, the cutoff frequency f_c does not prove satisfactory. This will be different in the aircraft case, since the characteristic distances of the reflections differ – more on this in Chapter 5. Also, the predicted carrier phase multipath content builds up from

the low frequencies to a sharp drop (see Figure 4.11) which is not coherent with the experimental PSD results (*c.f.*, the next section), where the multipath frequency content is much smoother. Therefore, further work is needed to refine the Jacobi-Anger validation method, starting with the definition of an actual quantitative threshold instead of validating f_c visually. In the remainder of this thesis, results are presented for $f_c = 9.55 \times 10^{-4}$ Hz.

Inputting the filter cutoff frequency from Equation 2.6 into a custom Matlab high pass filtering algorithm and using the filter on the single differentiated DF data theoretically yields carrier phase multipath-only data. In other words, the selected cutoff frequency is such that the filtering operation does not remove a significant amount of carrier phase multipath content from the DF single difference. For comparison, and according to the necessary scaling derived in Appendix C, Figure 4.12 provides a superposition of the DA and DF filtered with τ_c carrier phase multipath errors. Note that this comparison is only provided to get a rough reference for the DF carrier phase multipath. In reality, DA characterized carrier phase multipath cannot be used as a precise reference for DF carrier phase multipath since the DA involves two GNSS antennas in a short baseline configuration where multipath may cancel out because the environment as seen by each antenna is nearly identical.

Figure 4.12 shows that DF carrier phase multipath has a slightly greater variance than DA carrier phase multipath – with comparable frequency content. The slight difference in variance was to be expected, as per the probable cancelling out of the DA carrier phase multipath from the short baseline configuration of the antennas.

4.3.4 Frequency-domain bounding. Once the data has been mapped, and the windowing algorithm provided all the stationary sub-samples, the idea is to take the PSD of each of them separately, and then find a model that bounds all of them at the same time, like in the DA case. The three selectable bounding parameters

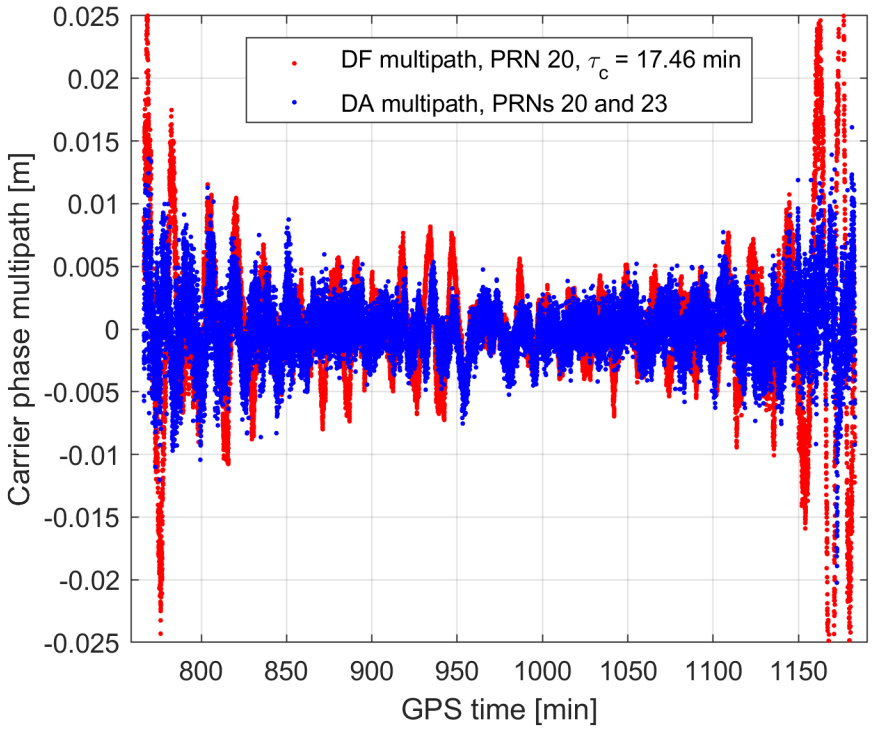

Figure 4.12. DA and DF multipath (scaled)

$\tau_{GM}^{(DF)}$, $\sigma_{GM}^{(DF)}$ and $\sigma_{WN}^{(DF)}$ values for the overall upper bound of all DF filtered single differences are provided in Equation 4.3, and the DF carrier phase multipath PSD bound is presented in Figure 4.13.

$$\begin{cases} \tau_{GM}^{(DF)} = 70 \text{ [s]} \\ \sigma_{GM}^{(DF)} = 4.0 \text{ [cm]} \\ \sigma_{WN}^{(DF)} = 0.9 \text{ [cm]} \end{cases} \tag{4.3}$$

Let us compare Figures 4.6 and 4.13, and GMRP parameters 4.1 and 4.3. Figure 4.14 provides a side-by-side, same scale comparison of both DA and DF PSD data and upper bounds. The PSD bound in the DF case has greater values for variance parameters than the PSD bound in the DA case – which is not surprising, as already mentioned. However, the $\sigma_{GM}^{(DF)}$ and $\sigma_{WN}^{(DF)}$ seem too high compared to what was to be expected (closer to 1 or 2 cm). This needs to be further explored. Three main

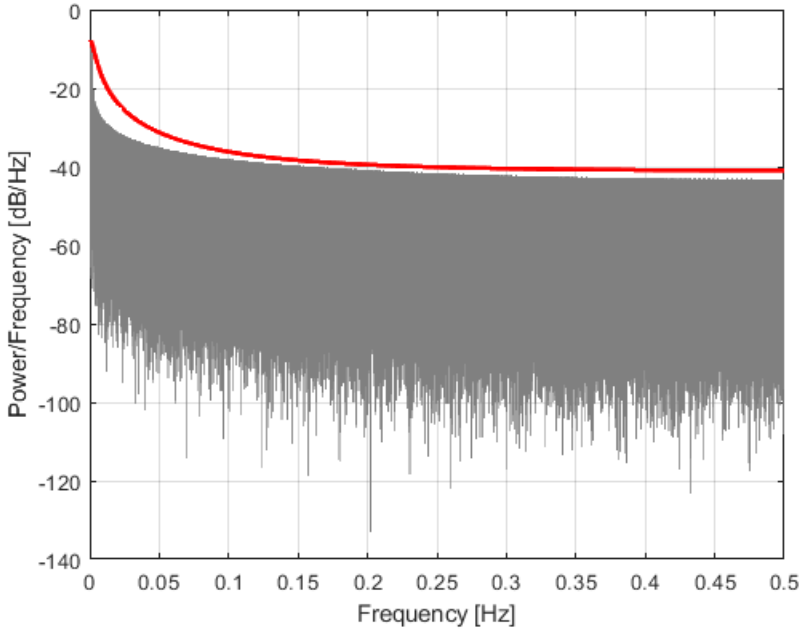

Figure 4.13. DF PSD bounded carrier phase multipath and GMRP upper bound

possible causes for these high bounding values (if they turn out not to be inherent from the data) are spectral leakage, filter type influence, and residual ionospheric delay. Spectral leakage comes from the window used during the computation of the PSD, when taking the Fourier transform of the ACF of the data (see Chapter 3). The shape of the window adds some undesired power content for some frequencies, which shows in the PSD. The filter type used for ionospheric delay removal might also have an influence on the power content, depending on which filtering function is used. Residual ionospheric delay could be spotted by refining the LS PSD method, by investigating the higher frequency content and comparing it to the LS PSD of unfiltered carrier phase data – and by using real ionospheric delay data such as IGS ionosphere products [22]. Investigating those possible causes will be the focus of future work. Note that the PSD upper bounds presented in this work (for either method) are not optimized in any way, and that there is no criteria on the tightness of the bounds. Further work may entail such an optimization method.

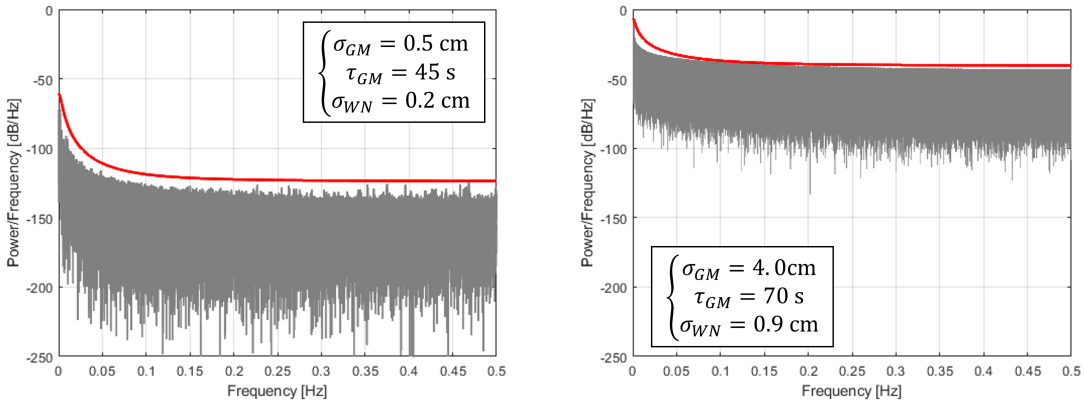

(a) DA PSD upper bound

(b) DF PSD upper bound

Figure 4.14. DA and DF carrier phase multipath GMRP upper bound

CHAPTER 5

METHODOLOGY FOR AIRCRAFT DATA APPLICATION

In this chapter, recommendations for application of the DF carrier phase multipath characterization and upper bounding methods to aircraft multipath are provided, including directions for the computation of the ionospheric delay filter cutoff frequency f_c.

5.1 Expectations

Multipath observed in data collected onboard an aircraft will be different from multipath seen in rooftop data presented in the previous chapter. The most evident source of aircraft multipath would come from the GNSS signal reflections from the plane itself: fuselage, wings (including winglets and mobile parts such as slats, flaps, spoilers, and engines, etc.) and tail structures (stabilizers, rudder, etc.). Figure 5.1 illustrates a very simple aircraft multipath example. There may also be multipath from the reflections on the ground and airport infrastructures during takeoff and landing procedures.

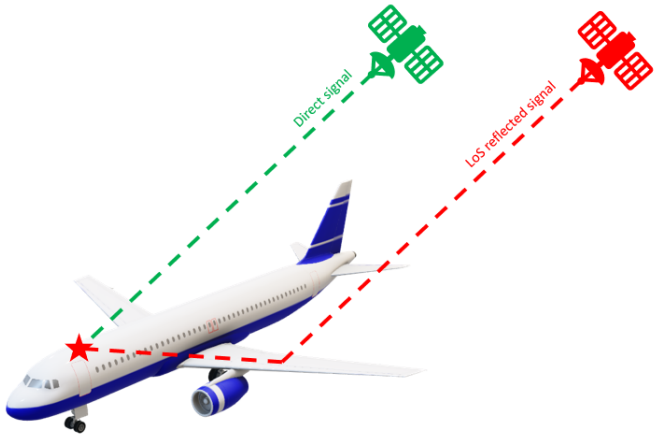

Figure 5.1. Aircraft multipath example

5.2 Ionospheric delay on a worldwide scale

For the rooftop data experiment, a local ionospheric delay filter cutoff frequency was computed – and this value is theoretically only valid for the Chicago, IL area. Therefore, worldwide values need to be computed, for the cutoff frequency to be valid along any flight path followed during airborne data collection. For that, in this work, a set of 20 ground stations homogeneously distributed are considered. Their locations can be seen on Figure 5.2, and their coordinates are reported on Table C.1 in Appendix C.

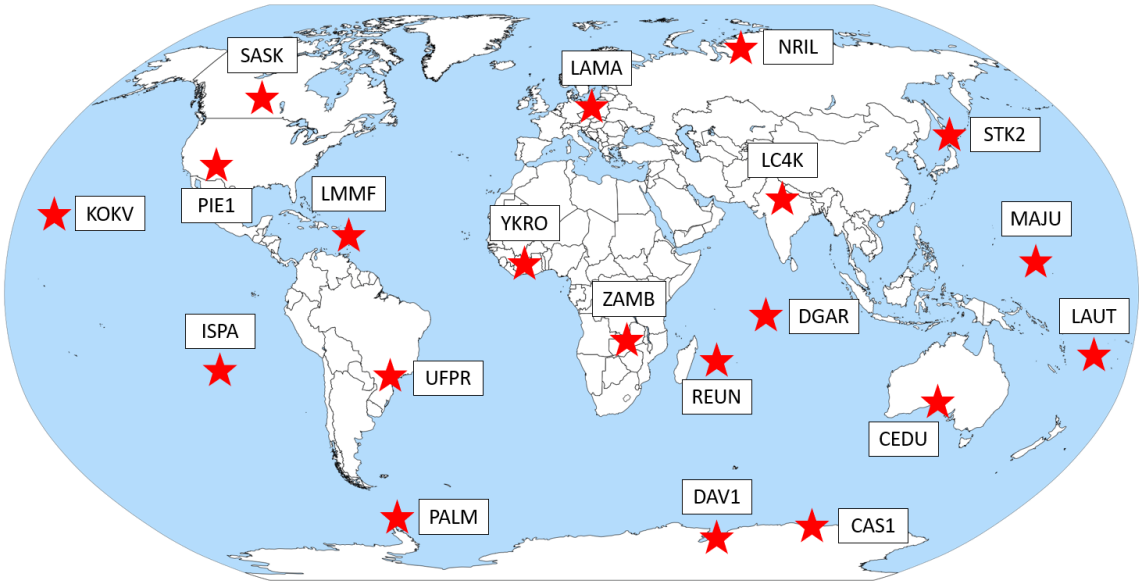

Figure 5.2. Ground stations

The ionospheric delay has already been simulated for both $L1$ and $L2$ frequencies for one day per month of the year 2020, and for each healthy satellite in view – this means that simulation data (about 7,000 data files) is ready available for further studies. The days of year chosen are the same as for the days chosen for the local time constant – *i.e.*, Monday of the first full week of each month. That way, a map of cutoff frequencies to be used for ionospheric delay filtering can be created, with a domain of validity for each frequency – at a given position, use the cutoff frequency from the

nearest station. Another approach would be to compute the cutoff frequency at set intervals in time for the coordinates of the airplane used for data collection, since an airplane is moving over time. While the IRI-based Fortran/Matlab code [13] used to compute ionospheric delay accounts for the movement of satellites, it currently only considers a fixed user (as described in Chapter 2). However, a moving user – an airplane – has a impact on the LoS change over time, as can be seen on Figure 5.3. Two options can be considered to solve this issue: either use a different ionospheric model than IRI that accounts for moving objects, or further modify the currently used Matlab script based on reference [13] to include target movement. Either one of these options would be acceptable, but in practice, computing the cutoff frequency for Earth fixed coordinates may be sufficient, since accounting for a moving user will probably add ionospheric delay dynamics that should be at lower frequencies than aircraft multipath. In fact, ground speed will probably not add multipath dynamics for an aircraft, but rather shift the observed ionospheric delay frequencies observed from said aircraft. This remains to be proven. Future work might want to focus on how to evaluate the impact of a moving user on ionospheric delay natural frequencies, since these frequencies may depend on the direction of movement (*i.e.*, if the aircraft moves following a satellite or not).

To get greater coverage and more precise values of the cutoff frequencies to use in the ionospheric delay filter, the number of fixed stations for which the ionospheric delay data is computed can be increased from the initial 20 stations suggested. The simulation can also be run on a greater number of days – the best being for each day of the considered year, but note that computation time would be considerably lengthened. Note that repeating the ionospheric data as mentioned in Chapter 4 before taking the LS PSD to compute the natural frequencies of the ionospheric delay phenomenon is recommended.

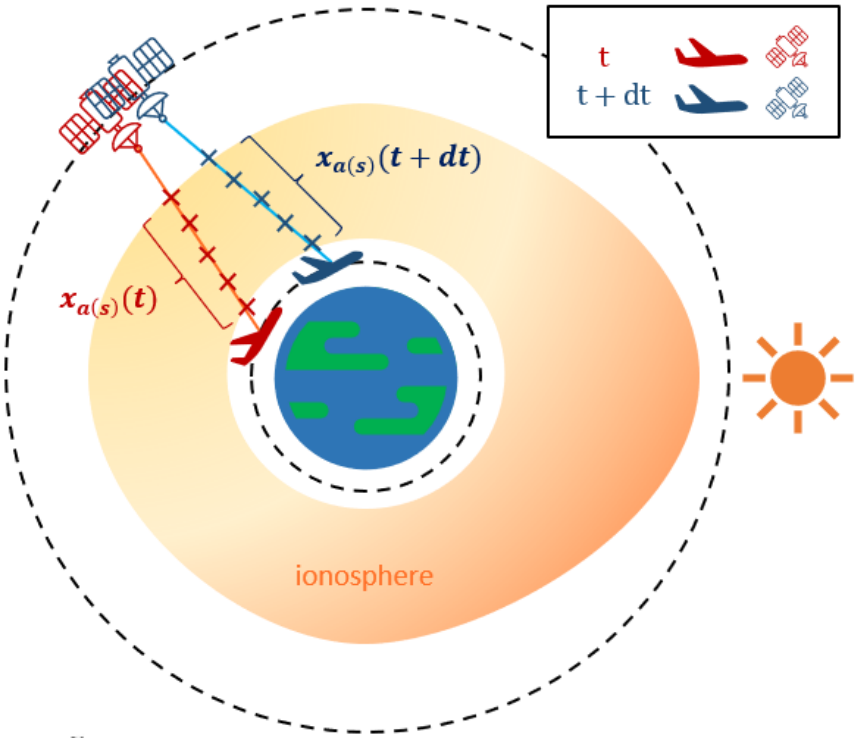

Figure 5.3. Slant ionospheric delay interpolation – moving user

5.3 Multipath variations from aircraft dynamic modes

In the case of aircraft carrier phase multipath, the notable multipath dynamics impacting carrier phase measurements, other than satellite movement, are the aircraft dynamic modes. To make sure that the high pass filter method for ionospheric delay removal can be used, the slowest aircraft dynamics need to be compared to the ionospheric time constant to ensure little or no multipath information is filtered out along with ionospheric delay. Only the slowest dynamics need to be considered because their frequency will be the closest to the ionospheric filter cutoff frequency f_c. Therefore, there is a higher probability that carrier phase multipath content originating from those slow dynamics is going to be filtered out. The slowest dynamics are observed in the biggest airplanes – for airliners, that encompasses, among others, the famous Boeing 747 and Airbus A380. Among of the biggest planes are also cargo aircraft. An aircraft in flight is free to rotate about three axes – its principal axes.

Those three principal axes, and motion about these axes are called yaw, pitch and roll (see Figure 5.4). The roll and pitch motions are widely called bank and heading motions, respectively. All airplanes have oscillatory modes about these axes [23] that can have a direct impact on multipath dynamics. The dynamic modes are represented and explained on Figure 5.6. Note that the pure yaw mode (greyed out on Figure 5.6) is in practise never observed on its own but always in combination with the pure roll mode – this mode is called the Dutch roll mode.

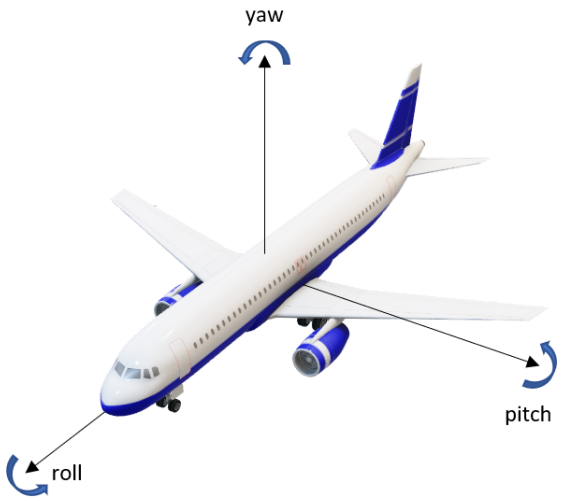

Figure 5.4. Yaw, pitch and roll axes and motions

In this section, dynamic modes frequencies for the Boeing 747-200 are used. Though it is not the biggest plane in service, information and dynamic stability studies on this model are widely available in the literature [24]. Dynamic stability studies for other plane models would be needed for validation of the DF carrier phase multipath characterization method on those aircraft. Consider the slowest longitudinal and lateral modes for the Boeing 747-200 – respectively phugoid and spiral divergence modes. The former has frequency $f_{ph} \approx 5.5 \times 10^{-3}$ Hz and the latter $f_{sp} \approx 3.1 \times 10^{-3}$ Hz [24]. To validate each local filter cutoff frequency, following the method described in Section 2.6 using the Jacobi-Anger expansions is recommended,

using the lowest frequency of all dynamic modes, and GNSS orbital periods, which are different depending on the considered GNSS constellation, as mentioned earlier.

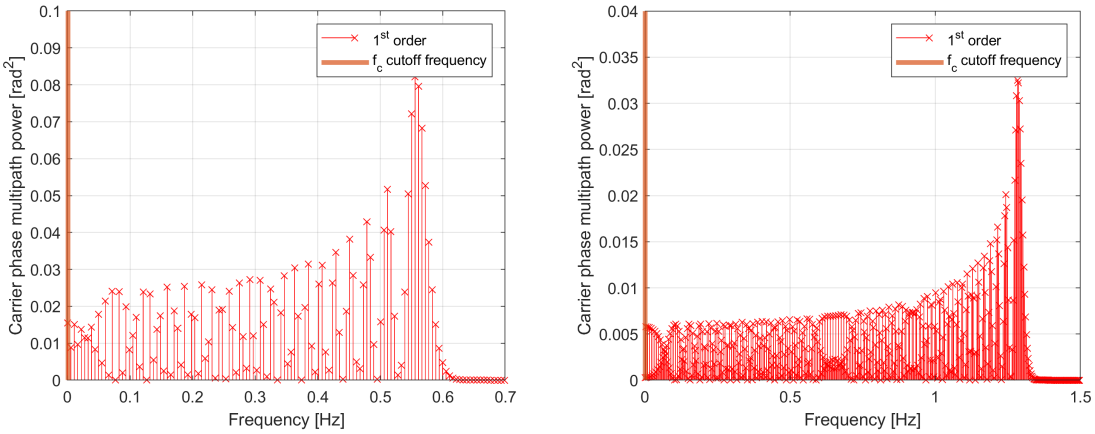

(a) Phugoid mode

(b) Spiral divergence mode

Figure 5.5. f_c validation though Jacobi-Anger expansion – Boeing 747-200 modes

Figure 5.5 provide the visuals for the ionospheric delay filter cutoff frequency validation on aircraft dynamic modes, using f_c computed in Chapter 4 for the Chicago area. The phugoid mode being a longitudinal mode, the verification is done using the ground reflection case, with $h = 10$ m (reflection near the root of the wings on the fuselage). The spiral mode being a lateral mode, the verification is done using the wall reflection case, with $d = 40$ m (reflection from potential winglets at the wingtips). From the two subfigures, this cutoff frequency can be validated, as it removes less than 1% of the multipath content. However, as mentioned before, there is no quantitative threshold on this validation, so designing one is left for future work. Note that with the aircraft natural frequencies being faster than the GPS orbit frequency, this validation is theoretically not essential. However, validating f_c on multipath frequencies due to satellite movement is challenging, since the relevant distances to consider change with airplane orientation. Therefore, further investigating the validation method and its application to aircraft is essential.

5.4 Dual Frequency (DF) method for aircraft multipath

The preferred method for aircraft carrier phase data processing and PSD bounding is the DF method. This is because some aircraft do not have two embedded GNSS antennas. And for those that do, using the DA method would require heavy real-time computations and precise tracking of the lever arm between the two antennas, which is involved in the geometric term of the double difference Equation 2.3. Also, if all the GNSS antennas are in the same local area on the aircraft in a short baseline configuration, then some of the multipath would probably cancel out. In addition, if there are multiple embedded GNSS antennas, it is more relevant to use them separately for redundancy. Therefore, the DF method seems more appropriate for carrier MP estimation. The required data for the DF method to be performed consists of raw carrier phase measurements, as well as their time of collection, and satellite orbit data. Aircraft attitude and ground speed information would be needed as well, for the ionospheric delay filter cutoff frequency computation and validation. Any combination of two carrier frequencies can be used – for instance, GPS $L1$ and $L2$ as in this work, or $L1$ and $L5$, for GPS again.

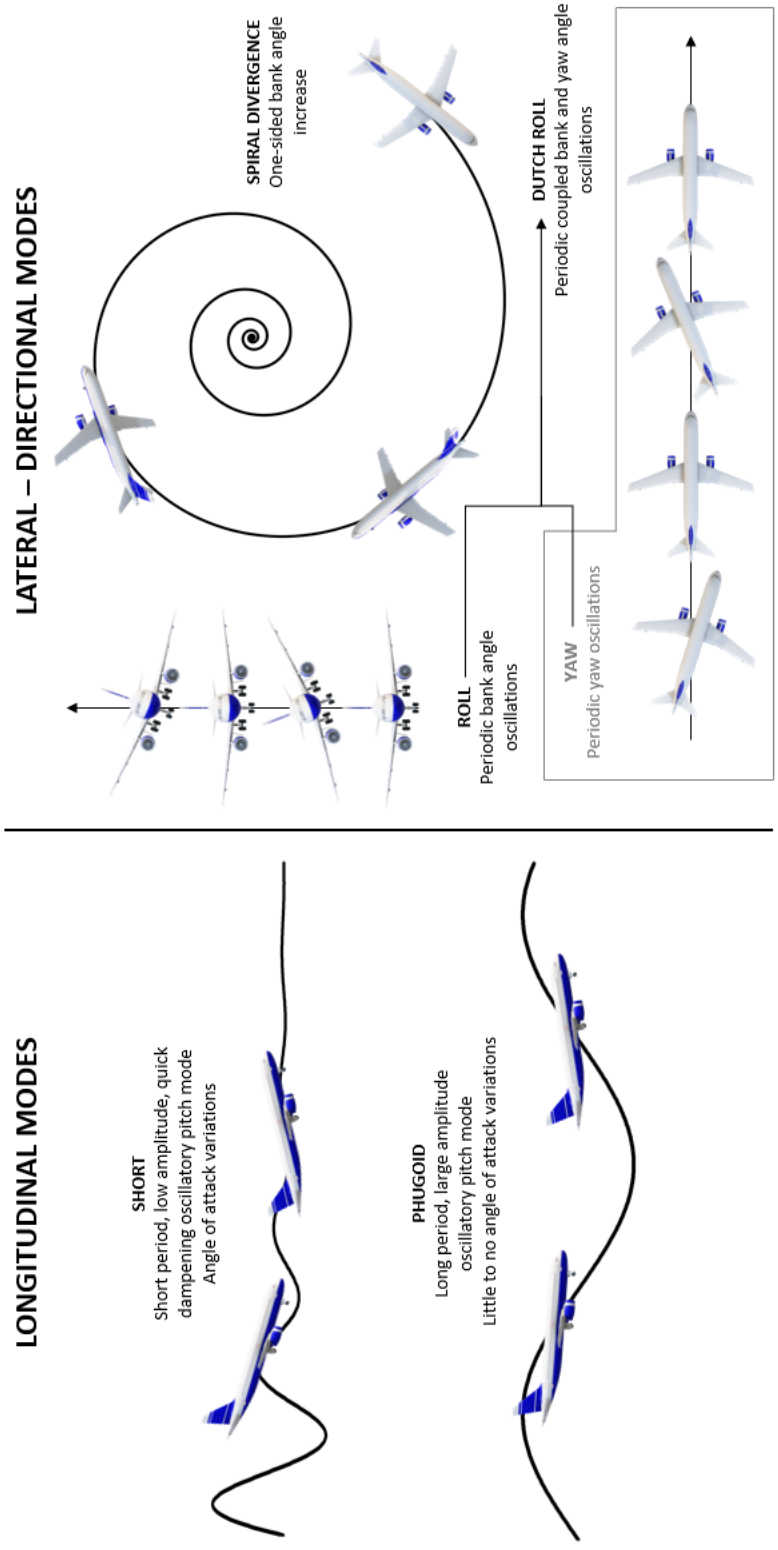

Figure 5.6. Aircraft dynamic modes

CHAPTER 6

CONCLUSION

6.1 Summary of contributions

This work provides a robust characterization and bounding model for DF multipath error for use in GNSS sensor fusion algorithms, including potential future implementations of ARAIM, complementing the results from references [6] and [5] characterizing tropospheric delay and orbit and clock errors in the frequency domain. To build up the necessary tools required for the DF method, as well as to provide a rough estimation of what can be expected, the DA method was first tested, since it is already widely used. But for numerous reasons provided early in this thesis the DF method is preferred over the DA method for aircraft carrier phase multipath characterization and PSD bounding – hence the DF method is the core focus of this work. Single differencing carrier phase measurements over two frequencies leaves a composite term containing DF multipath, ionospheric delay and cycle ambiguity – the latter two needing to be removed. To solve this issue, this work discusses the feasibility and details of ionospheric delay high pass filtering, whose cutoff frequency is computed using estimations from the well known IRI ionospheric model.

Once the the methodology for ionospheric filter cutoff frequency is selection and validation was developed, two options were considered. The first one was based on time domain filtering of the ionospheric delay, then bounding the DF multipath in the PSD domain. The second option relied on first converting the data to the frequency domain using an appropriate function (the LS PSD), and then filter the ionospheric delay directly in the frequency domain. Each one has its advantages and drawbacks, but reasons were given for why it is best to rely on the first option.

As a benchmark test case, carrier phase measurements collected using rooftop antennas were processed using both the DA and DF methods. In parallel, the iono-

spheric simulation was run to reproduce ionospheric delay dynamics using GPS satellite orbit data from almanacs broadcast during the year 2020. The simulation allowed to compute a value for the ionospheric delay filter cutoff frequency used in the DF method. To validate this cutoff frequency, a Bessel function expansion model was analytically derived.

Finally, as the DF method developed in this work is meant to be used with airborne collected data, considerations for further studies on actual aircraft carrier phase measurements were provided and discussed to allow for a quick adaptation of the algorithms developed for the rooftop benchmark case.

6.2 Considerations on iono free combination

Carrier phase iono-free combinations are already used in ARAIM. Therefore, ARAIM users would be more interested in an iono-free carrier phase multipath model than in the DF carrier phase multipath model developed in this work. However, characterizing iono-free carrier phase multipath from iono-free combination is shown to be more challenging. This is because iono-free combinations are frequency-scaled combinations of carrier phase measurements from two frequencies [11], meaning the iono-free combinations will contain most of the carrier phase error terms in Equation 2.1. Those error terms will need to be removed individually, either using external products (which would require a very precise knowledge of each term), or by filtering. Though filtering may be feasible for orbit and tropospheric delay errors, clock bias frequency characteristics are receiver dependent and extremely unpredictable. Therefore, filtering or predicting and removing this term would result in a model that is receiver-dependent and not generalizable. So, instead, the approach chosen for this work is to derive a DF carrier phase multipath characterization methods, with plans to relate these to the iono-free case in future work. It can be hoped that since iono-free combinations are frequency-scaled combinations of carrier phase measurements

from two frequencies [11], only mere scaling would be sufficient. This remains to be investigated and proven.

6.3 Future work

The following are recommendations for future work:

- Improve the PSD bound for DF carrier phase multipath by investigating possible causes of artificially added frequency content. As of now, thought of potential causes for the unsatisfactory GMRP PSD upper bound parameters are spectral leakage from the window used when taking the Fourier transform of the ACF during the PSD computation for the DF carrier phase multipath, ionospheric delay filter type, and non negligible ionospheric delay residual presence in the filtered data.

- Refine the ionospheric delay cutoff frequency computation method, especially if it does not provide satisfactory results when performed on stations all over the world, especially at high latitudes. Account for ground speed of aircraft. Also, validate this method on real ionospheric delay data.

- Refine the ionospheric delay cutoff frequency validation method, since it provided non satisfactory results in the rooftop benchmark case presented in this dissertation. Also, design a quantitative threshold for validation, and study the reflective environment of an aircraft for a more precise validation.

- Put the DF method to the test with aircraft carrier phase data.

- Study the link between the DF carrier phase characterization method – which was the main focus of this thesis – and DF carrier phase multipath from iono free combinations. Note that using different carrier frequencies combinations for the DF single difference and ionospheric delay study would probably change the

magnitude of the DF carrier phase single difference and estimated ionospheric delay, but not their dynamics.

- Extend the DF method to carrier phase measurements from other GPS frequencies and other GNSS constellations.

APPENDIX A

GPS SIGNAL GROUND REFLECTION

This appendix is dedicated to showing that the real case presented on Figure 2.3 for the signal extra travelled distance is equivalent to the virtual antenna case presented on Figure A.1.

A.1 Virtual antenna case

From Figure A.1, it is straightforward that:

$$\Delta = 2d \sin\theta \tag{A.1}$$

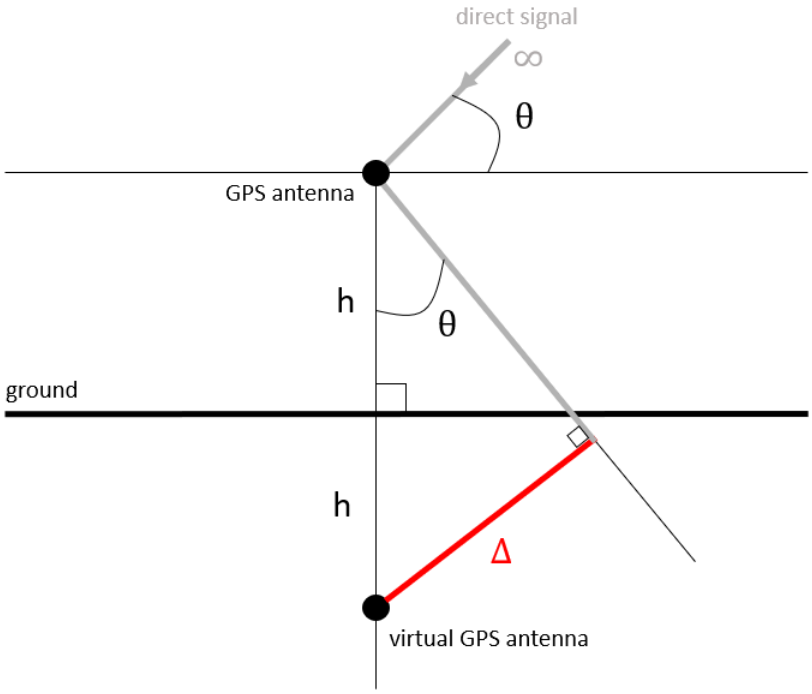

Figure A.1. GPS signal ground reflection – virtual antenna simplification

A.2 Real case

From Figure 2.3, $\Delta = \Delta_1 - \Delta_2$ is the extra distance travelled by the reflected signal before reaching the antenna. The two following relationships can be easily derived:

$$\begin{cases} d = \Delta_1 \sin\theta \\ \Delta_2 = \Delta_1 \cos(2\theta) \end{cases} \tag{A.2}$$

From there, an expression for Δ is obtained:

$$\Delta = \Delta_1 - \Delta_2 = \frac{d}{\sin\theta}(1 - \cos(2\theta)) \tag{A.3}$$

Then, by using the trigonometric identities $\cos(2\theta) = (1 - \sin^2\theta)$ and $\cos^2\theta + \sin^2\theta = 1$, the final expression is:

$$\Delta = 2d\sin\theta \tag{A.4}$$

This expression is equal to the simpler virtual antenna case presented in previous section.

APPENDIX B

DUAL ANTENNA (DA) AND DUAL FREQUENCY (DF) MULTIPATH RESULTS SCALING

Before comparing results from both DA and DF methods, scaling of both carrier phase residuals is needed. Equations 2.3 and 2.4 give the expressions for the multipath estimated with the Dual Antenna and Dual Frequency methods. Both carrier phase residuals can be thought of as being distributed as a sum of normal random variables. The estimated multipath from frequency f, satellite s and antenna a at time k can be modeled as:

$$\nu_{a(s)}^{t(f)} \sim \mathcal{N}(\mu_{a(s)}^{(f)}, \sigma_{a(s)}^{(f)}) \tag{B.1}$$

Hence, the estimated multipath from the DA method can be written:

$$\nu_{a_1-a_2(s_1-s_2)}^{k(L1)} \sim \mathcal{N}(\mu_{DA}, \sqrt{{\sigma_{a_1(s_1)}^{(L1)}}^2 + {\sigma_{a_2(s_1)}^{(L1)}}^2 + {\sigma_{a_1(s_2)}^{(L1)}}^2 + {\sigma_{a_2(s_2)}^{(L1)}}^2}) \tag{B.2}$$

and the estimated multipath from the DF method can be expressed:

$$\nu_{a_1(s_1)}^{k(L1-L2)} \sim \mathcal{N}(\mu_{DF}, \sqrt{{\sigma_{a_1(s_1)}^{(L1)}}^2 + {\sigma_{a_1(s_1)}^{(L2)}}^2}) \tag{B.3}$$

Equation B.4 holds true from the short baseline property:

$$\sigma_{a_1(s_1)}^{(L1)} = \sigma_{a_2(s_1)}^{(L1)} \text{ and } \sigma_{a_1(s_2)}^{(L1)} = \sigma_{a_2(s_2)}^{(L1)} \tag{B.4}$$

Equation B.5 holds true assuming multipath from all satellites is taken from a common distribution:

$$\sigma_{a_1(s_1)}^{(L1)} = \sigma_{a_1(s_2)}^{(L1)} \text{ and } \sigma_{a_2(s_1)}^{(L1)} = \sigma_{a_2(s_2)}^{(L1)} \tag{B.5}$$

Hence, from Equations B.4 and B.5:

$$\sigma_{a_1(s_1)}^{(L1)} = \sigma_{a_1(s_2)}^{(L1)} = \sigma_{a_2(s_1)}^{(L1)} = \sigma_{a_2(s_2)}^{(L1)} \tag{B.6}$$

Assuming that the multipath phenomenon is not frequency dependant:

$$\sigma_{a_i(s_i)}^{(L1)} = \sigma_{a_i(s_i)}^{(L2)} \; \forall i \in \{1, 2\} \tag{B.7}$$

Thus, naming σ_{DA} and σ_{DF} the measured standard deviations for the characterized multipath from respectively DA and DF methods:

$$\sigma_{DA} = 2\sigma^{(L1)}_{a_1(s_1)} \text{ and } \sigma_{DF} = \sqrt{2}\sigma^{(L1)}_{a_1(s_1)} \tag{B.8}$$

Hence, for the results to be comparable, the multipath error isolated with the dual antenna method must be divided by 2 and the multipath from the dual frequency method must be divided by $\sqrt{2}$. Note that this holds true for any other carrier frequencies combinations, not only $L1$-$L2$.

APPENDIX C

REFERENCE GROUND STATIONS FOR THE COMPUTATION OF WORLDWIDE IONOSPHERIC DELAY TIME CONSTANT

Table C.1. Ground stations coordinates in decimal degrees

Identifier	Latitude	Longitude	Identifier	Latitude	Longitude
LC4K	26.91	80.96	**STK2**	43.53	141.84
CEDU	-31.87	133.81	**DAV1**	-68.58	77.97
DGAR	-7.27	72.37	**KOKV**	22.13	-159.66
PALM	-64.78	-64.05	**YKRO**	6.87	-5.24
MAJU	7.12	171.36	**UFPR**	-25.45	-49.23
NRIL	69.36	88.36	**LAMA**	53.89	20.67
CAS1	-66.28	110.52	**SASK**	52.20	-106.40
REUN	-21.21	55.57	**PIE1**	34.30	-108.12
ZAMB	-15.43	28.31	**LAUT**	-17.61	177.45
ISPA	-27.12	-109.34	**LMMF**	14.59	-61.00

BIBLIOGRAPHY

[1] S. Bancroft, "An algebraic solution of the GPS equations," in *IEEE Transactions On Aerospace and Electronic Systems*, pp. 56–59, 1985.

[2] E. Kaplan and C. Hegarty, *Understanding GPS: principles and applications*. Artech House, 2nd ed., 2006.

[3] G.-H. Ji, K.-H. Kwon, and J.-H. Won, "GNSS signal availability analysis in SSV for geostationary satellites utilizing multi-GNSS with first side lobe signal over the Korean region," *Remote Sensing*, vol. 13, 2021.

[4] "International Reference Ionosphere." http://irimodel.org/, Last accessed: 01/15/2022.

[5] E. Gallon, M. Joerger, and B. Pervan, "Frequency-domain modeling of orbit and clock errors for sequential positioning," in *2020 IEEE/ION Position, Location and Navigation Symposium (PLANS)*, pp. 239–246, 2020.

[6] E. Gallon, M. Joerger, and B. Pervan, "Robust modeling of GNSS tropospheric delay dynamics for sequential positioning," in *Proceedings of the 33rd International Technical Meeting of the Satellite Division of The Institute of Navigation (ION GNSS+ 2020)*, pp. 1041–1053, 2020.

[7] Y. Morton, F. van Diggelen, J. Spilker, and B. Parkinson, *Position, Navigation, and Timing Technologies in the 21st Century: Integrated Satellite Navigation, Sensor Systems, and Civil Applications*, vol. 1. Wiley, 2021.

[8] "GPS: The global positioning system." https://www.gps.gov/systems/gps/, Last accessed: 03/28/2022.

[9] P. Misra and P. Enge, *Global Positioning System: Signals, Measurements, and Performance*. Ganga-Jamuna Press, 2nd ed., 2006.

[10] G. Maral and M. Bousquet, *Satellite Communications Systems: Systems, Techniques and Technology*. Wiley, 2002.

[11] A. Leick, L. Rapoport, and D. Tatarnikov, *GPS Satellite Surveying*. Wiley, 4th ed., 2015.

[12] C. Altman and K. Suchy, *Reciprocity, Spatial Mapping and Time Reversal in Electromagnetics*. Kluwer Academic Publishers, 1991.

[13] S. Stevanovic, M. Joerger, S. Khanafseh, and B. Pervan, "Atomic clock aided receiver for improved GPS signal tracking in the presence of wideband interference," in *Proceedings of the 28th International Technical Meeting of the Satellite Division of The Institute of Navigation (ION GNSS+ 2015)*, pp. 3296–3306, 2015.

[14] J. VanderPlas, "Understanding the Lomb–Scargle periodogram," *The Astrophysical Journal Supplement Series*, vol. 236, p. 28, 2018.

[15] M. Abramovitz and I. Stegun, *Handbook of Mathematical Functions*. Dover Publications, Inc., 1972.

[16] C. Chatfield, *The Analysis of Time Series – An Introduction*. Chapman and Hall, 4 ed., 1989.

[17] O. Garcia Crespillo, M. Joerger, and S. Langel, "A new approach for modeling correlated Gaussian errors using frequency domain overbounding," in *2020 IEEE/ION Position, Location and Navigation Symposium, PLANS 2020*, pp. 868–876, 2020.

[18] A. Piersol and J. Bendat, *Random data : analysis and measurement procedures*. Wiley, 2nd ed., 2011.

[19] H. Levene, "Robust tests for equality of variances," in *Contributions to Probability and Statistics*, pp. 278–92, 1960.

[20] J. Pratt and J. Gibbons, "Kolmogorov-Smirnov two-sample tests," in *Concepts of Nonparametric Theory*, pp. 318—-344, Springer, 1981.

[21] O. Garcia Crespillo, M. Joerger, and S. Langel, "Overbounding GNSS/INS integration with uncertain GNSS Gauss-Markov error parameters," in *2020 IEEE/ION Position, Location and Navigation Symposium (PLANS)*, pp. 481–489, 2020.

[22] "International GNSS Service." https://igs.org/products/#ionospheric_products, Last accessed: 04/15/2022.

[23] L. Schmidt, *Introduction to Aircraft Flight Dynamics*. American Institute of Aeronautics and Astronautics, Inc., 1998.

[24] T. Ogunwa and E. Abdullah, "Flight dynamics and control modelling of damaged asymmetric aircraft," in *IOP Conference Series Materials Science and Engineering*, p. 012022, 2016.